Semarak Engineering Journal

Journal homepage:
https://semarakilmu.my/index.php/sej/index
ISSN: 3036-0145

A Compact X-Band Radar Beamforming MIMO Antenna with a Modified 4x4 Butler Matrix

Yusnita Rahayu[1,*], Faril Pirwanhadi[1], Ahmad Al-Alif[1], Ery Safrianti[1], Dian Widiastuti[2], Mudrik Alaydrus[2], Huanyu Larry Cheng[3]

[1] Department of Electrical Engineering, Universitas Riau, Pekanbaru 28293, Indonesia
[2] Department of Electrical Engineering, Universitas Mercu Buana, Jakarta, Indonesia
[3] Department of Materials Science and Engineering, The Pennsylvania State University, Pennsylvania 16802, The United States of America

ARTICLE INFO

Article history:
Received 10 March 2026
Received in revised form 13 May 2026
Accepted 10 July 2026
Available online 9 August 2026

Keywords:
Butler Matrix, Multi-Beam Antenna Array, MIMO Antenna, X-band, Beam Forming

ABSTRACT

Indonesia's vast maritime territory requires compact, mobile, smart radar antenna systems for effective security monitoring. This study evaluates 4x4 MIMO array antennas with conventional and modified Butler matrices, assessing crossover reduction's effect on S-parameters and radiation patterns. The conventional design achieves higher peak gains (11.9 dBi edge, 9.75-9.76 dBi middle) than the modified design (10.7-10.8 dBi), though the modified matrix offers more consistent return loss (-12.5 dB) versus -10.6 dB (middle) and -27.3 dB (edge) for the conventional design. Isolation performance differs by port location: the modified matrix improves edge-port isolation (-12.9 to -21.2 dB, S14/S41) relative to the conventional design (-6.3 dB), while its middle-port isolation (-7.2 dB, S23/S32) is weaker than the conventional design's (-12.8 to -15 dB), indicating a redistribution rather than a uniform improvement. Despite a flipped middle-phase response from the crossover omission, the modified matrix retains functional radiation patterns. These results show that the modified design achieves a more compact, balanced configuration with improved edge-port isolation and return loss, but at the cost of lower peak gain and larger tilt-angle deviation (±3° versus ±2°) compared to the conventional design. Beyond simulation, a fabricated 2x2 MIMO array with a 2x2 Butler matrix was measured via VNA, confirming beam-steering at 340.39° and 31.36° and validating the crossover-reduction approach in hardware.

1. Introduction

In recent years, usage of X-band frequencies within wireless communication networks has grown significantly [1]. X-band radar systems are widely deployed on large research vessels and various offshore installations. Originally designed for purposes such as ship traffic management and navigation, these systems have been adapted with specialized hardware and software enhancements, enabling their application in the measurement of waves and currents [2]. Furthermore, various governments have recognized the potential of X-band frequencies and have

[*] *Corresponding author.*
E-mail address: yusnita.rahayu@lecturer.unri.ac.id

https://doi.org/10.37934/sej.15.1.199234

begun allocating portions of this spectrum for commercial use [3], creating new opportunities for service providers aiming to enhance network infrastructure and deliver better services to customers.

The X-band frequency occupies a crucial segment of the electromagnetic spectrum within the microwave radio domain. Operating in the 8-12 GHz range, with a wavelength of 2.4-3.75 cm [4], the X-band falls under the Super High Frequency (SHF) category, making it ideal for supporting land, sea, and air communications, particularly for voice, image, data, and high-definition video transmission. Under severe weather conditions, X-band signals exhibit reduced atmospheric attenuation, making them a preferred choice for satellite communications [5].

Radio Detection and Ranging (Radar) technology has evolved since the late 19th century, with its conceptual roots stemming from Heinrich Hertz's experiments in the 1880s, which sought to validate James Clerk Maxwell's electromagnetic radiation theory. Maxwell's contributions in formulating electromagnetic field equations allowed for a more comprehensive understanding of the relationship between light and radio waves as manifestations of electromagnetic phenomena, albeit within different frequency regimes [6].

As the world's largest archipelago state, Indonesia, with a total territorial area of 8.300.000 km^2, of which 6.400.000 km^2 comprises water [7], requires an effective defense and security system to safeguard its territory. Radar technology plays a crucial role in this system. Despite the continuous advancements in radar technology, its core principle, applied across all generations of radar systems, whether Continuous-Wave (CW) or Ground-Controlled Interception (GCI), remains consistent with the radar range equation. This equation forms the foundation of radar technology development, as range is a critical aspect of any radar system's operation, particularly for object detection [8].

Previous research on Butler matrix technology has explored various approaches in the development of intelligent radar antennas and beamforming systems. For instance, Ding *et al.* [9] proposed a 6x6 beamforming network incorporating 3x3 and 2x2 hybrid couplers with quasi-arbitrary phase differences. Their design demonstrated a significant enhancement in the capacity of beamforming technology, which is crucial for improving radar performance and signal clarity [9]. Similarly, Rahayu and Simanihuruk [10] developed a 4x4 Butler matrix integrated with 5G antennas that operates at 38 GHz, highlighting the practical applications of beamforming in modern 5G communication systems. This design showcases how beamforming can optimize signal directionality and bandwidth in high-frequency networks [10]. In another study, Liu *et al.* [11] employed the Monte Carlo method to simulate variations in beamforming patterns resulting from fluctuations in amplitude, phase, or both. Their findings revealed that phase fluctuations in the communication channel had a more profound effect at the angle in the main lobe, rather than on the variations in amplitude, underscoring the importance of phase control for accurate and efficient beamforming [11]. Furthermore, Rahayu *et al.* [12] demonstrated improvements in antenna design efficiency by developing a 1x4 array antenna integrated with a 4x4 Butler matrix at 38 GHz, further advancing the precision of antenna arrays in beamforming applications [12]. Shao and Chen [13] extended this research by proposing a 2x8 Butler matrix with variable power distribution. Their design utilized 180° filtering screws and resonator-based power dividers to enable adjustable power distribution, phase shifting, and bandpass filtering, which significantly enhanced the flexibility and efficiency of beamforming systems. Collectively, these studies illustrate the recent advancements in Butler matrix design and its critical role in optimizing 5G communication and radar technologies [13].

In the realm of array antenna development, various approaches have been explored to enhance MIMO antenna performance. Rahayu [14] designed an 8x1 MIMO antenna specifically for the application of 5G technology, operating at 38 GHz. The simulation results demonstrated exceptional performance metrics, including a reflection coefficient (S11) of -29.5 dB, 13.44 dBi gain, and a 14.002 GHz bandwidth. Moreover, mutual coupling between antenna elements was maintained below -10 dB, ensuring minimal interference and optimal signal quality—an essential feature for high-efficiency communication systems [14]. Paul *et al.* [15] investigated high-gained microstrip array antennas for X-band radar applications, employing inset feeding techniques to enhance performance. Their 2x4 array antenna achieved 15.5 dB peak gain and a bandwidth of 380 MHz, while the 1x4 array demonstrated a half-power beamwidth of 16.88° and a bandwidth of 880 MHz. These designs, simulated using ANSYS HFSS, highlighted the effectiveness of microstrip arrays in achieving high gain and wide bandwidth, which are crucial for radar and communication systems [15]. Similarly, Phaneendra *et al.* [16] developed a 1x2 MIMO antenna for 4G and 5G networks, designed to operate at multiple frequencies, such as 9.3 GHz, 19.3 GHz, and 17.5 GHz. The antenna achieved -18 dB, -28 dB, and -29 dB reflection coefficients, with corresponding gains and impedance bandwidths of 5.22 dB and 1.24 GHz, 5.27 dB and 1.6 GHz, and 5.71 dB and 5.89 GHz, respectively. The consistency of these results highlights the antenna's reliability across different frequencies [16]. Additionally, Sahoo *et al.* [17] designed an array antenna operating at 28 GHz, available in various configurations, including 16x16, 8x8, 4x4, and 2x2. This versatile antenna design significantly enhances the performance of 5G MIMO wireless communication systems by improving spectral efficiency and energy efficiency, as well as reducing bit error rates. These improvements are essential for achieving higher data transmission rates and more reliable connections in modern communication networks. Collectively, these studies on array antenna development contribute valuable insights into enhancing the performance and scalability of MIMO and radar systems in both civilian and military applications [17].

The primary challenge in developing military radar antenna technology lies in addressing increasingly complex and dynamic threats. Advances in civilian and commercial radar technology also drive the need for enhancements in military radar capabilities. As a result, continuous development of military radar antennas is necessary to ensure they are adaptive, efficient, and responsive to evolving threats, to meet the demand expansion for security and defense.

A conventional 4x4 Butler matrix requires two crossover components to route signal paths between non-adjacent ports. Each crossover is conventionally realized by cascading two 3 dB hybrid couplers, which increases the overall circuit footprint, insertion loss, and phase deviation at the crossing lines [18, 19]. This added complexity limits the compactness and cost-effectiveness of the conventional design, particularly for applications where miniaturization is prioritized. To address this limitation, the modified Butler matrix presented in this study replaces one of the two crossover units with a single 2x2 hybrid coupler with an altered feedline and characteristic impedance, reducing the number of crossover components from two to one. This modification directly targets the size and complexity limitation of the conventional design, at the expense of introducing a flipped middle-phase response that must be accounted for in the array feed.

The contribution of this paper is to give an insight into the effect of minimizing the crossover element in conventional Butler matrix design in advance to make the configuration more compact. By comparing both configurations of S-parameter and far-field results, it is shown that the modified configuration provides a more compact, balanced configuration, with trade-offs discussed in Section 4. Additionally, the modified configuration has a smaller dimension of 84.565mm x 57.18mm compared to the 89.615mm x 57.18mm conventional configuration dimension.

The research aims to thoroughly investigate how these configurations can enhance the efficiency, accuracy, and adaptability of smart antenna systems, particularly in high-demand military applications. By offering a detailed examination of the performance metrics associated with these antenna systems, the study intends to offer valuable insights into potential improvements for current and future smart antenna designs.

Furthermore, this paper goes beyond simulation by fabricating and experimentally validating the design up to a 2×2 MIMO array antenna, both as a standalone array and integrated with a 2×2 Butler matrix, using Vector Network Analyzer (VNA) measurements. This provides a quantified comparison between simulated and measured reflection coefficients (S11), mutual coupling, and radiation pattern for each configuration, and identifies the likely physical causes of the observed deviation, including fabrication dimensional tolerance, connector/soldering imperfections, impedance mismatch, and the absence of an anechoic testing environment.

By combining simulation with physical fabrication and measurement, this research aims to establish how reliably a compact, crossover-reduced Butler matrix beamforming network translates from design to hardware, particularly for high-demand military and maritime surveillance radar applications. The measured beam-steering behavior obtained from the 2×2 array–Butler matrix prototype offers direct evidence that the phase-shifting network functions as intended outside of simulation, which is an essential step before scaling the same crossover-reduction approach to larger 4×4 and higher-order array configurations.

Ultimately, the findings from this study — spanning both simulated design and its experimental validation — are intended to inform the future development of larger, more complex Butler matrix–fed array antennas, contributing to the ongoing evolution of adaptive, compact smart antenna systems for radar technology.

2. Methodology

In the complex and multifaceted design of smart antennas specifically intended for radar applications, the development process is generally categorized into two key components: the design of MIMO antennas and the configuration of the Butler Matrix. Prior to addressing the technical intricacies of these designs, it is imperative to first select an appropriate substrate material for antenna construction. The selection of substrate material is crucial, as it has a profound impact on the overall performance of the antenna system, particularly in signal propagation, impedance matching, and efficiency.

For the design configurations, a substrate with a high dielectric constant and excellent stability is essential. Such a material helps to minimize the antenna dimensions while ensuring a compact radiation pattern, in line with the research objectives. In this study, the RT Duroid 3010 substrate is used, with 1.28 mm thickness, 10.2 dielectric constant, and 0.0021 tangent loss, as detailed in Table 1 [20].

Table 1
Material specifications of the substrate

Specification	Description
Substrate type	RT Duroid 3010
Relative dielectric constant (εr)	10.2
Tangent loss (tan δ)	0.0004
Substrate thickness (h)	1.28 mm

2.1 MIMO Antenna Configurations

In the initial phase of antenna design, dimensions are determined using theoretical principles and formulas. This section presents and analyzes the configurations of single-element antenna arrays, specifically 2x2 and 4x4, all operating within the X band.

The patch on the microstrip antenna serves as a radiation element that generates electromagnetic waves. Located on a dielectric substrate, these patches are typically made of conductive material such as copper and can have a variety of shapes, such as rectangles, triangles, or circles [18], as depicted in Figure 1. The primary function of a patch antenna is to transmit signals into the air and receive signals from the surrounding environment, making it a crucial component in wireless communication systems. The design characteristics of the patch, including its dimensions and the choice of substrate, significantly influence the antenna performance parameters, such as bandwidth, radiation patterns, and gain [19].

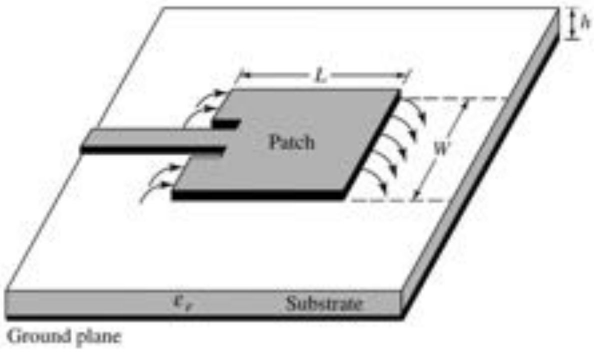

Fig. 1. Microstrip Line Feed

Detailed designs of these antenna configurations, with initial dimensions calculated using specific Eqs. (1-6), are outlined and discussed in the section from the previous study [18].

$$W_p = \frac{c}{2f}\sqrt{\frac{2}{\varepsilon_r+1}} \tag{1}$$

$$\Delta L = 0.412xh\left[\frac{(\varepsilon_{eff}+0.3)\left(\frac{W_p}{h}+0.264\right)}{(\varepsilon_{eff}-0.258)\left(\frac{W_p}{h}+0.8\right)}\right] \tag{2}$$

$$\varepsilon_{eff} = \frac{\varepsilon_r+1}{2}+\frac{\varepsilon_r-1}{2}\left[1+\frac{12h}{W_p}\right]^{-\frac{1}{2}} \tag{3}$$

$$L_p = \frac{c}{2f\sqrt{\varepsilon_{eff}}} - 2\Delta L \tag{4}$$

$$W_s = W_p + 6h \tag{5}$$

$$L_s = L_p + 6h \tag{6}$$

A microstrip line is a transmission structure consisting of a conductor placed on a dielectric substrate, with electric field characteristics influenced by fringing effects at the edges of the line [18], as presented in Figure 2. These fringing effects occur because the electric field is not fully confined within the substrate but spreads into the surrounding air, which can affect the characteristic impedance (Z0) of the microstrip line [21]. The dimension configuration of the microstrip line, including width (W) and substrate height (h), is crucial in design as they impact wave propagation and antenna performance, such as bandwidth and radiation efficiency. Therefore, understanding the relationship between microstrip line dimensions and substrate dielectric parameters is essential for designing effective communication systems [22].

Fig. 2. Microstrip line

To find the dimensions of the microstrip line, Eqs. (7-12) below can be used [18].

$$W_f = \frac{2h}{\pi}\left(B - 1 - ln\ (2B-1) + \frac{\varepsilon_r - 1}{2\varepsilon_r}\left(ln\ (B-1) + 0.39 - \frac{0.61}{\varepsilon_r}\right)\right) \tag{7}$$

$$B = \frac{377\pi}{2Z_0\sqrt{\varepsilon_r}} \tag{8}$$

$$\varepsilon_{eff} = \frac{\varepsilon_r + 1}{2} + \frac{\varepsilon_r - 1}{2}\left[1 + \frac{12h}{W_f}\right] \tag{9}$$

$$\Delta L = \frac{\lambda_0}{\sqrt{\varepsilon_{eff}}} \tag{10}$$

$$\lambda_0 = \frac{c}{f} \tag{11}$$

$$L_f = \frac{\Delta L}{4} \tag{12}$$

2.1.1 Single Element Antenna

Using the equations explained in the methodology, the antenna dimensions are determined based on theoretical principles. However, to achieve optimal results, several adjustments are made, such as modifying the shape of the patch and the substrate. In a single-element antenna, only 1 microstrip antenna is displayed, where the design that has been characterized has a return loss below -10 dB and has a directional radiation pattern. Characterization results from antenna dimensions are depicted in the following Table 2.

Table 2
Dimension parameter of single-element antenna

Dimension	Size (mm)
Substrate thickness (h)	1.28
Patch thickness (t)	0.035
Patch width (w_P)	6.5
Patch length (l_P)	6.83
Feed width (w_f)	1.2
Feed length (l_f)	3.6
Inset feed length (y_0)	2.5

By using these parameters, a single-element antenna can be designed according to Figure 3.

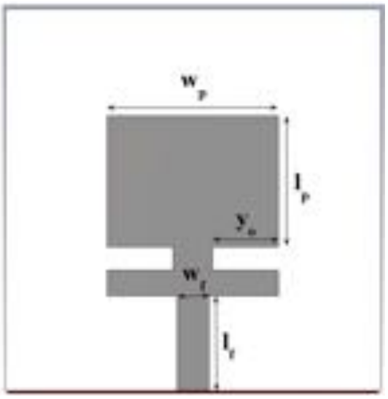

Fig. 3. Design configuration of single-element antenna

2.1.2 2x2 MIMO Antenna

In designing the 2x2 MIMO antenna, two rows and two columns of single-element antennas are arranged, resulting in a total of four patch antennas. The anticipated outcome is comparable to that of a single-element antenna, but with the added benefit of a narrower beam direction, resulting in a higher gain than the single-element configuration. Figure 4 illustrates the structure of the 2x2 MIMO antenna.

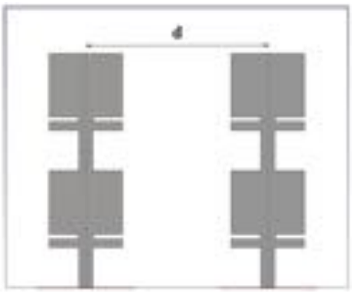

Fig. 4. Design configuration of 2x2 MIMO antenna

The designs and dimensions of the 2x2 MIMO antenna are presented in Figure 4, as well as in Table 3. The spacing between antenna elements (d) in the array is set at λ/2, equivalent to 10.43 mm, measured from the center of one element to the center of the next. However, after further characterization, the element spacing was adjusted to 16.2 mm.

Table 3
Dimension parameter of 2x2 MIMO antenna

Dimension	Size (mm)
Substrate thickness (h)	1.28
Patch thickness (t)	0.035
Patch width (w_P)	6.5
Patch length (l_P)	6.83
Feed width (w_f)	1.2
Feed length (l_f)	3.6
Inset feed length (y_0)	2.62
Distance between patches (d)	16.2

2.1.3 4x4 MIMO Antenna

In the design of a 4x4 MIMO antenna, four rows and four columns of single-element antennas are arranged, resulting in a total of sixteen patch antennas. The expected performance is similar to single-element and 2x2 MIMO antennas but with the added advantage of a narrower beam direction, leading to a higher gain than both the single-element and 2x2 MIMO configurations. Figure 5 illustrates the structure of the 4x4 MIMO antenna.

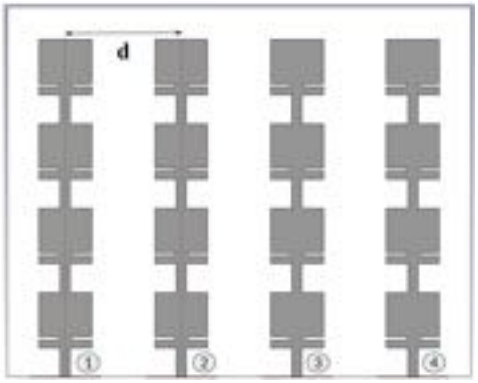

Fig. 5. Design configuration of 4x4 MIMO antenna

The designs and dimension configuration of the 4x4 MIMO antennas are illustrated in Figure 5 and Table 4. In the antenna array, the spacing between the individual antenna elements (denoted as d) is initially set at $\lambda/2$, which corresponds to a distance of 10.43 mm. This measurement is taken from the center of one antenna element to the center of the adjacent element. However, following a comprehensive characterization process, it was determined that the optimal element spacing needed adjustment. Consequently, the spacing was revised to 14.3 mm to enhance performance and meet design specifications.

Table 4
Dimension parameter of 4x4 MIMO antenna

Dimension	Size (mm)
Substrate thickness (h)	1.28
Patch Thickness (t)	0.035
Patch width (w_P)	6.5
Patch length (l_P)	6.83
Feed width (w_f)	1.2
Feed length (l_f)	3.6
Inset feed length (y_0)	2.5
Distance between patches (d)	14.3

2.2 Butler Matrix Configuration

Butler Matrix consists of a hybrid coupler, phase shifter, and crossover circuit. These components work together to enable the formation of multiple beams, each oriented in a distinct, fixed direction. The hybrid coupler is responsible for splitting and combining signals, while the phase shifter adjusts the phase of the signal, and the crossover circuit facilitates signal routing between different paths. Figure 6 provides a detailed schematic of the Butler Matrix used in this research, illustrating the arrangement and interaction of these components, as referenced from prior studies [23].

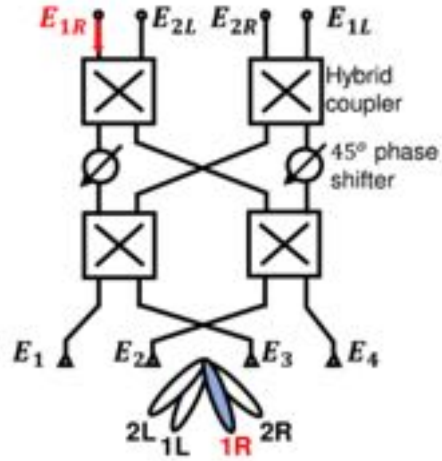

Fig. 6. Butler matrix general anatomy

The calculation of the antenna dimensions begins with the determination of key parameters essential for the design, including the desired operating frequency (f), substrate thickness (h), and dielectric constant (ε_r) of the substrate. Subsequently, the impedance configuration (Z_n) from each path is analyzed to establish the dimensions of the components within the Butler matrix. Figure 7 illustrates the dimensional parameters based on the conventional 2x2 hybrid coupler structure [24].

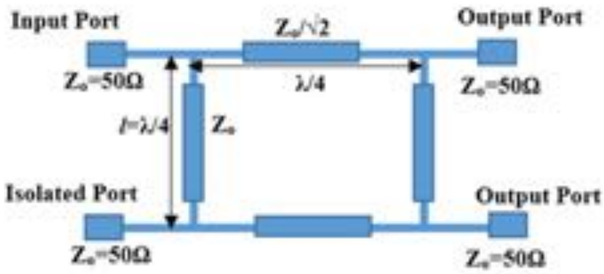

Fig. 7. Structure of 2x2 conventional hybrid coupler

Based on the conventional 2x2 hybrid coupler structure in Figure 7, the size configuration applies to all components of the Butler matrix, which consists of microstrip lines that have an impedance Z0 of 50 Ω, and the 2x2 Hybrid Coupler line has an impedance $Z_0/\sqrt{2}$ of 70.711 Ω. But specifically for the phase shifter, there is one additional parameter to determine the phase shifter path length (α) that will affect the phase shift. In advance, Figure 8 shows where the path length is located on the phase shifter, which will affect the phase shift.

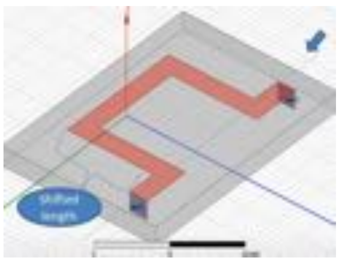

Fig. 8. Phase shifter structure.

To determine the initial dimensions of the coupler element, specific Eqs. (13-18) are employed, as detailed in previous studies [24-27].

$$\varepsilon_e = \frac{\varepsilon_r+1}{2} + \frac{\varepsilon_r-1}{2}\left(\frac{1}{\sqrt{1+10\frac{h}{W}}}\right) \tag{13}$$

$$\lambda = \frac{c}{f\sqrt{\varepsilon_e}} \tag{14}$$

$$Z_n = \begin{pmatrix} \frac{60}{\sqrt{\varepsilon_e}} ln\left(\frac{8d}{W} + \frac{W}{4h}\right) & for\frac{W}{h} \le 1 \\ \sqrt{\varepsilon_e}\left[\frac{W}{h} + 1.393 + 0.667ln\left(\frac{W}{h} + 1.444\right)\right] & for\frac{W}{h} \ge 1 \end{pmatrix} \tag{15}$$

$$\frac{W}{h} = \begin{pmatrix} \frac{8e^A}{e^{2A}-2} & for\frac{W}{h} < 2 \\ \frac{2}{\pi}\left[B - 1 - ln\,(2B-1) + \frac{\varepsilon_r+1}{2\varepsilon_r}\left\{ln\,(B-1) + 0.39 - \frac{0.61}{\varepsilon_r}\right\}\right] & for\frac{W}{h} > 2 \end{pmatrix} \tag{16}$$

$$A = \frac{Z_0}{60}\sqrt{\frac{\varepsilon_r+1}{2}} + \frac{\varepsilon_r-1}{\varepsilon_r+1}\left(0.23 + \frac{0.11}{\varepsilon_r}\right) \tag{17}$$

$$\alpha = \theta\frac{\lambda}{360} \tag{18}$$

In microstrip technology, designing a complete circuit often requires the strip path to make sharp turns. A sudden 90° bend in the microstrip results in the majority of the signal being reflected to the source, with only a small portion transmitted through the bend. This occurs because the bend causes a small accumulation of positive and negative charges on the surface of the transmission line, which increases the capacitance and alters the impedance of the line. These impedance changes cause a mismatch in the load, resulting in a portion of the signal on the line being reflected to the source, thereby reducing the overall system performance. Therefore, it is necessary to eliminate this unwanted capacitance development when the transmission line is bent. A mitered bend is one of the bending methods carried out by cutting the curved end of the transmission line at a certain angle to minimize VSWR, insertion loss, and return loss, and to minimize capacitance so that the characteristic impedance can return to its original state [18]. Figure 9 shows the parameter configuration of the mitered bend.

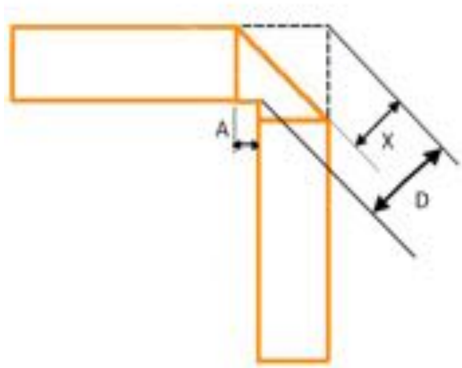

Fig. 9. Mitered bend configuration on microstrip.

Formulas for determining the initial dimensions of the coupler elements can be found in Eqs. (19-21) [26].

$$D = W\sqrt{2} \tag{19}$$

$$X = W\sqrt{2}\left(0.52 + 0.65e^{\left(-1.35\frac{W}{h}\right)}\right) \quad (20)$$

$$A = \left(X - \frac{D}{2}\right)\sqrt{2} \quad (21)$$

To assist in the calculations, Table 5 shows a summary of the initial parameters known from the design. Based on Table 5, other parameter calculations can be performed. Table 6 shows the calculation results of other parameter calculations obtained from equations (6), (14), (15), (17), and (18), along with the order of performing parameter calculations in stages.

Table 5
Summary of initial parameters of Butler matrix

Calculation Parameter	Antenna Specification
c	2.998 x 10^8 m/s
f	9.3 GHz
ε_r	10.2
h	1.28 mm
Z_0	50 Ω

Table 6
Summary of advanced parameters of Butler matrix

Calculation Stage	Calculation Parameter	Value
I	A	2.17
	B	3.708
II	W/h	0.938 mm
	W	1.2 mm
III	ε_e	20.421
IV	λ	10.093 mm

2.2.1 2x2 Hybrid Coupler

The 2x2 hybrid coupler, also known as a -3 dB coupler or branch-line coupler, is designed to evenly split input power into two equal output powers. In theory, a hybrid coupler should distribute half of the power for each output, while introducing a 90° phase difference between them [19]. However, simulation results often show minor deviations from the ideal -3 dB due to inherent losses in the system [9]. Figure 10 shows the structure of the 2x2 hybrid coupler.

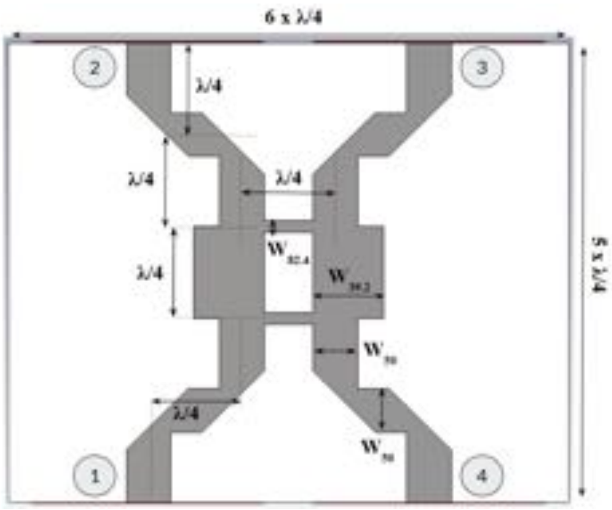

Fig. 10. Dimensional configuration of 2x2 hybrid coupler

For the design configuration of the 2x2 hybrid coupler, the circuit also functions as a 2x2 Butler Matrix. Table 7 provides the dimensional parameters of the 2x2 hybrid coupler configuration and its associated impedance, as determined by Eq. (3). Table 8 serves as a size guideline for the design. The 2x2 hybrid coupler is designed to evenly distribute the input power between the two output ports while simultaneously functioning as a 2x2 Butler Matrix.

Table 7
Dimensional Parameters of 2x2 Hybrid Coupler

Characterized Impedance (Z_n)	**W_n (mm)**	**L_n (mm)**
Z_{50}	1.2	3.084
$Z_{82.4}$	0.3265	3.222
$Z_{39.2}$	1.9	3.021

Table 8
Dimensional Configuration of the 2x2 Hybrid Coupler

Parameter	**Dimension (mm)**
λ/4	2.525
W_{50}	1.2
$W_{82.4}$	0.3265
$W_{39.2}$	1.9

2.2.2 Crossover

The second major component developed is the crossover as part of the 4x4 Butler matrix. This element is typically constructed by combining two 3 dB couplers [20]; however, this design achieved a smaller dimension that only includes a single 2x2 hybrid coupler with an altered feedline and characteristic impedances. The crossover reduces the impact of coupling power from hybrid couplers. Hence, the crossover achieves a power of 0 dB at the crossed line. Furthermore, the crossover is meant to ensure significant isolation loss at the other two crossing lines, preventing any electrical connection between them [19]. Figure 11 illustrates the structure of the proposed crossover.

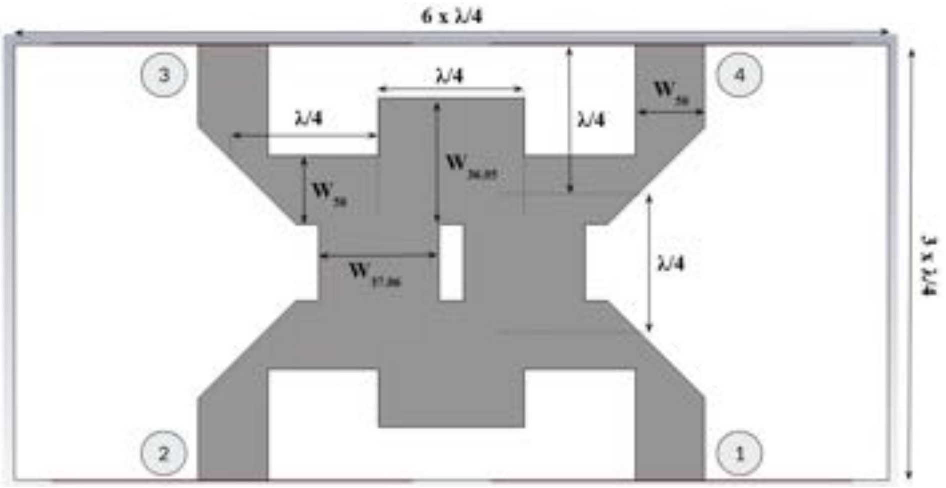

Fig. 11. Dimensional configuration of proposed crossover

For the design configuration of the crossover, Table 9 shows the dimensional parameters of the crossover configuration and its characterized impedance, which involves (3), and Table 10 is used as a size guideline in the design.

Table 9
Dimensional Parameters of Crossover

Characterized Impedance (Z_n)	W_n (mm)	L_n (mm)
Z_{50}	1.2	3.084
$Z_{36.05}$	2.2	3
$Z_{37.06}$	2.1	3.006

Table 10
Dimensional Configuration of the Crossover

Parameter	Dimension (mm)
λ/4	2.525
W_{50}	1.2
$W_{36.05}$	2.2
$W_{37.06}$	2.1

2.2.3 Phase Shifter

A phase shifter comprises a transmission line segment of predetermined length, designed to impart a specified phase shift to a signal [19]. In this research, 135°, 180°, and 0° phase shifters were designed and utilized in two configurations of a 4x4 Butler matrix: a conventional design and a modified version. The phase shifters were tailored based on their neighboring connections to ensure the correct matching of the output phase shift. Specifically, the 135° and 180° phase shifters were employed to compensate for the 135° phase shift introduced by the crossover network, achieving a 0° output and 45° output, respectively. Additionally, the 0° phase shifter was implemented to calibrate for a 0° output, compensating for phase discrepancies arising from the MIMO antenna patch distance. Figure 12 depicts the configurations of phase shifters.

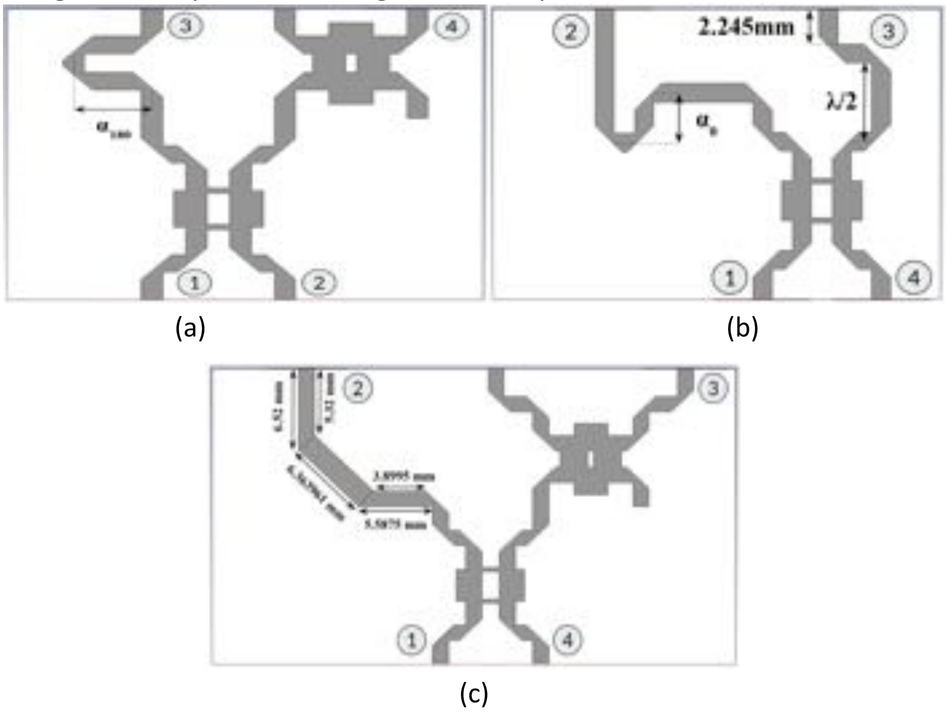

(a) (b) (c)

Fig. 12. Dimensional configuration of phase shifter: (a) 0°, (b) 180°, and (c) 135°

In advance of phase shifter design configuration, the calculation of phase shifter dimensions involves equation (7), while the calculation of the dimensions of the mitered bend involves equations (8), (9), and (10). In addition, the microstrip line configuration uses the Z_{50} characterization impedance, so that the microstrip has a path with a width of 1.2 mm with a path length of 3.084 mm. The microstrip line configuration will be used in the mitered bend calculation parameters. Table 11 shows the dimensional calculation parameter data on the phase shifter and mitered bend configurations, and Table 12 is used as a size guideline in the design.

Table 11
Dimensional Parameters of Phase Shifter

Configuration	Calculation Parameter				
Phase Shifter	θ_0	α_0	θ_{180}	α_{180}	W_{50}
	0°	3.185 mm	180°	4.514 mm	1.2 mm
Mitered Bend	D	X	A		
	1.697 mm	1.194 mm	0.488 mm		

Table 12
Dimensional Configuration of the Phase Shifter

Parameter	Dimension (mm)
λ/4	2.525
W_{50}	1.2
α_0	3.185
α_{180}	4.514
A	0.488

2.2.4 4x4 Butler Matrix

The study's 4x4 Butler matrix design integrates four 2x2 hybrid couplers, crossover units, two phase shifters, and two microstrip lines with a characteristic impedance of 50 Ω. Figure 13 depicts both the conventional and modified designs of the Butler matrix, showcasing dimensional configurations. The modified design omits a crossover unit, altering the size and signal path.

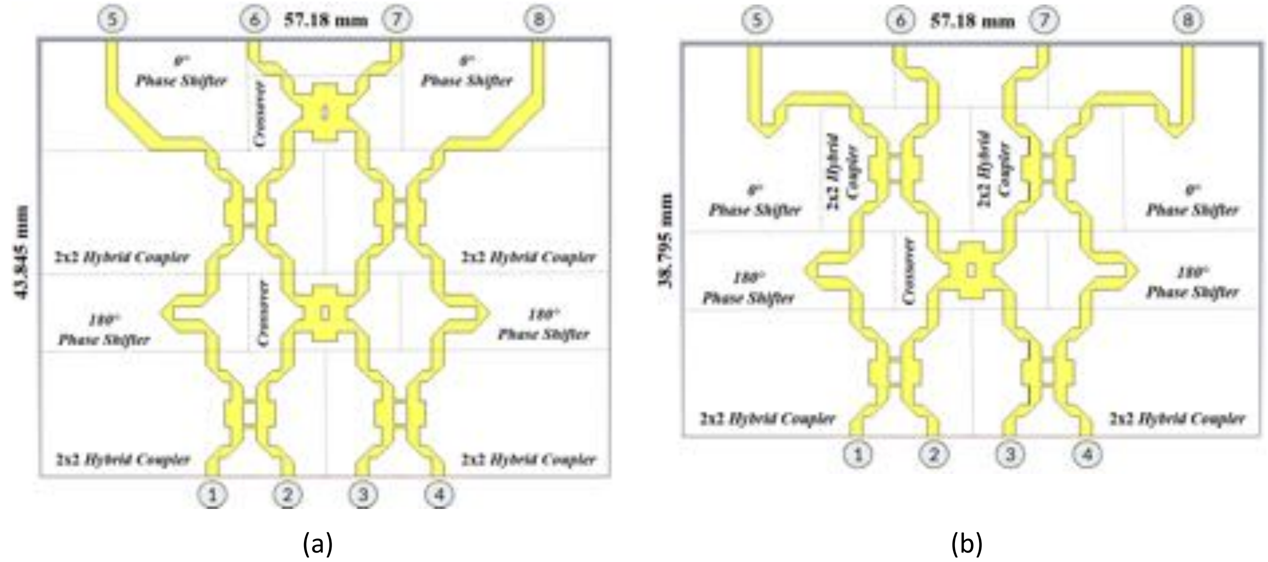

Fig. 13. Design and dimensional configuration of 4x4 Butler matrix: (a) conventional, and (b) modified version

Table 13 further quantifies the dimensions in millimeters, emphasizing key parameters found in Figure 13.

Table 13
Dimensional configuration of the 4x4 Butler matrix

Parameter	Dimension (mm)
λ/4	2.525
W_{50}	1.2
L_{50}	3.084

2.3 Design Integration

Figure 14 illustrates the schematic integration of a 2x2 MIMO array antenna with a 2x2 Butler matrix. This smaller-scale configuration serves as a baseline for validating the beamforming and phase-shifting performance of the Butler matrix network before extending the analysis to the larger 4x4 configuration, and later provides the reference design for the physical fabrication and measurement stage.

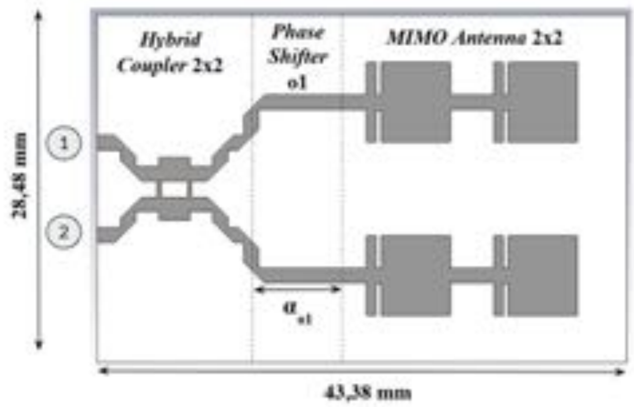

Fig. 14. Schematic diagram of the integrated 2×2 MIMO array antenna and 2×2 Butler matrix configuration

Figure 15 illustrates the schematic integration of a 4x4 MIMO array antenna with the conventional Butler matrix. This configuration optimizes signal distribution and phase adjustment for effective comparison with the modified version.

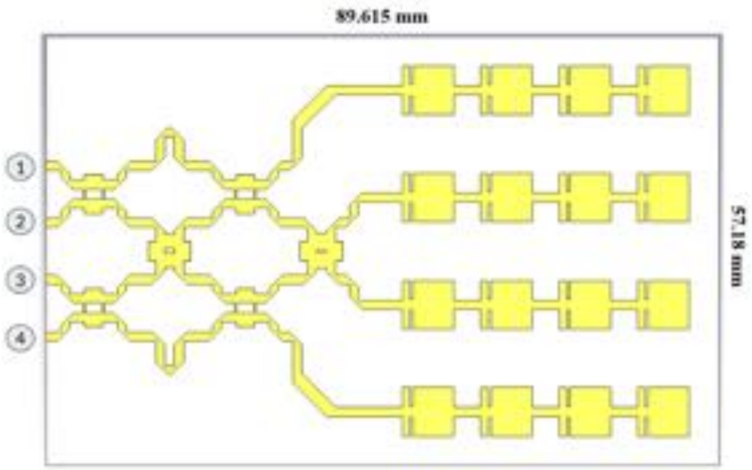

Fig. 15. Schematic diagram of the integrated 4x4 MIMO array antenna and conventional 4x4 Butler matrix configuration

Similarly, Figure 16 highlights the structural modifications in the integrated design, which adapts to the omission of the crossover unit. Both schematics emphasize the system's structural and functional differences, aiding in beamforming and signal management.

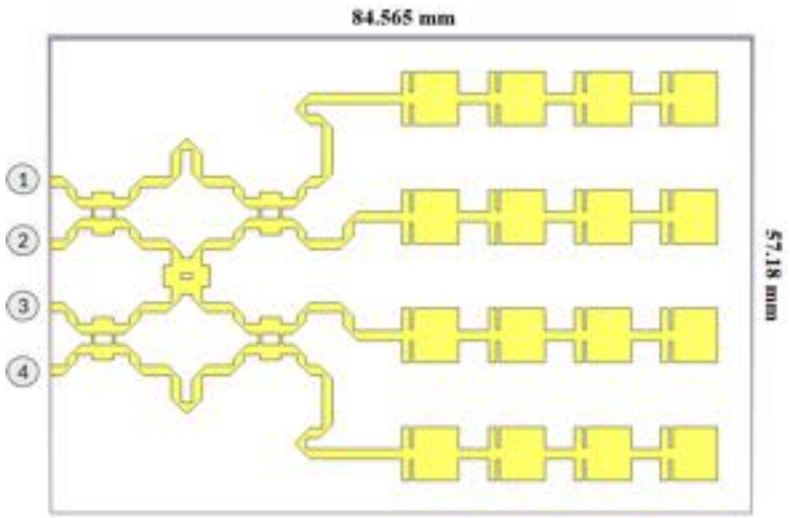

Fig. 16. Schematic diagram of the integrated 4x4 MIMO array antenna and modified 4x4 Butler matrix configuration

2.4 Measurement Setup

The antenna performance was experimentally characterized using a Vector Network Analyzer (VNA), specifically the ZVA 67, to measure the reflection coefficient (S-parameters) across the designed operating frequency range. The primary objective of this measurement was to evaluate the practical performance of the fabricated antenna and to facilitate a direct comparison with the corresponding simulation results. In addition, radiation pattern measurements were conducted for each antenna configuration using the same measurement setup. The complete antenna measurement procedure is illustrated in Figure 17.

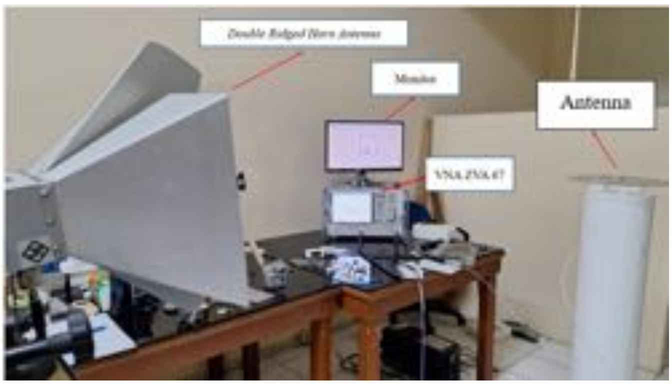

Fig. 17. Measurement setup for antenna

It should be noted that all measurements were performed in an open, non-shielded environment rather than within an anechoic chamber. Consequently, the measurement results may be affected by external electromagnetic interference, multipath propagation, and signal reflections from surrounding objects. These environmental factors are considered when analyzing the discrepancies observed between the simulated and measured antenna performance.

3. Results

The simulation results of the integrated 4x4 MIMO array antennas with their corresponding 4x4 conventional and modified Butler matrices are demonstrated by both the S-parameter performance and radiation pattern characteristics.

3.1 Single Element Antenna

The simulation results of the single-element antenna show that the design gives a reflection coefficient of -48.328 dB at 9.3 GHz. The antenna exhibits a bandwidth of 110 MHz within the X-band frequency range, suitable for radar applications. Figure 18 shows simulated results of S-parameters of the single-element antenna.

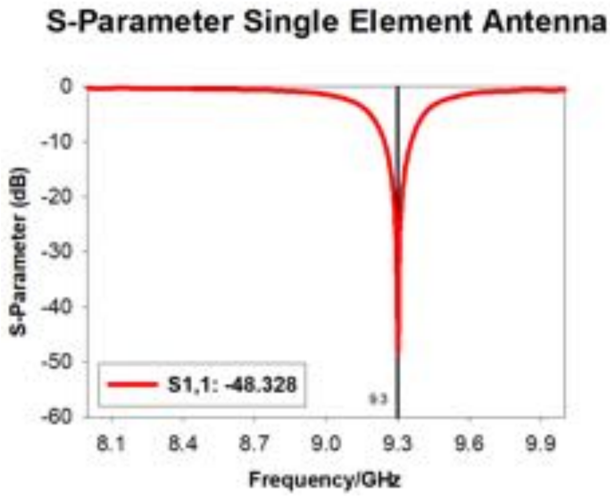

Fig. 18. Simulation result of the reflection coefficient of the single-element antenna

Additionally, far-field or radiation pattern results of the single-element antenna show that the main beam gain at its peak is recorded at 3.03 dBi or 2.01 W/m^2 at 9.3 GHz. This simulated result underscores its potential for targeted signal transmission and is used as the foundation for further configurations. Figure 19 shows simulated far-field results of a single-element antenna.

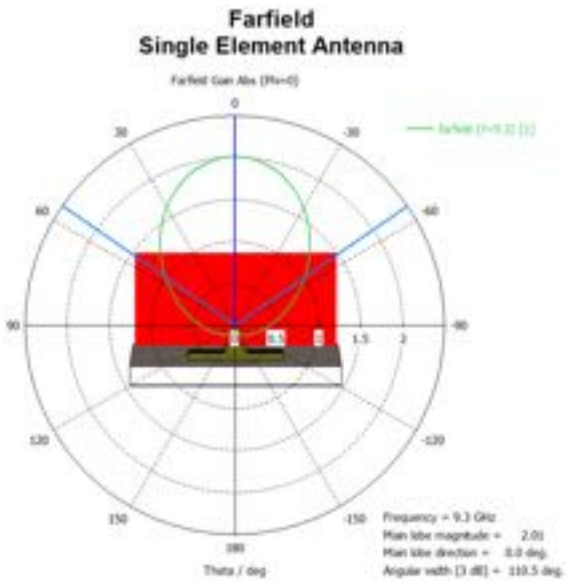

Fig. 19. Simulated far-field result for π = 0° from single element antenna at Y=-0.1 and Z=1

3.2 2x2 MIMO Antenna

The 2x2 MIMO antenna, simulated as an arrangement of four single-element antennas, shows promising performance at 9.3 GHz. The simulation results of the 2x2 MIMO antenna show -20.982 dB and -27.451 dB for ports 1 and 2, respectively, at 9.3 GHz, while isolation values between the ports exceed -20 dB, highlighting effective signal separation. Figure 20 shows simulated results of S-parameters of a 2x2 MIMO antenna.

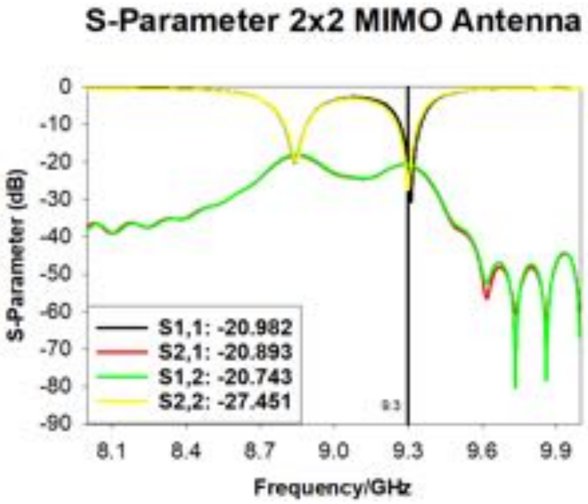

Fig. 20. Simulation result of 2x2 MIMO antenna

Additionally, far-field or radiation pattern results of the 2x2 MIMO antenna show that the main beam gain at its peak is recorded at 5.65 dBi or 3.68 W/m^2 for port 1 excitation and 5.61 dBi or 3.64 W/m^2 for port 2 excitation at 9.3 GHz. This simulated result underscores its potential for targeted signal transmission, showing both ports have similar radiation patterns with the same position, and are used as the continuation for further configurations. Figure 21 shows simulated far-field results of a 2x2 MIMO antenna.

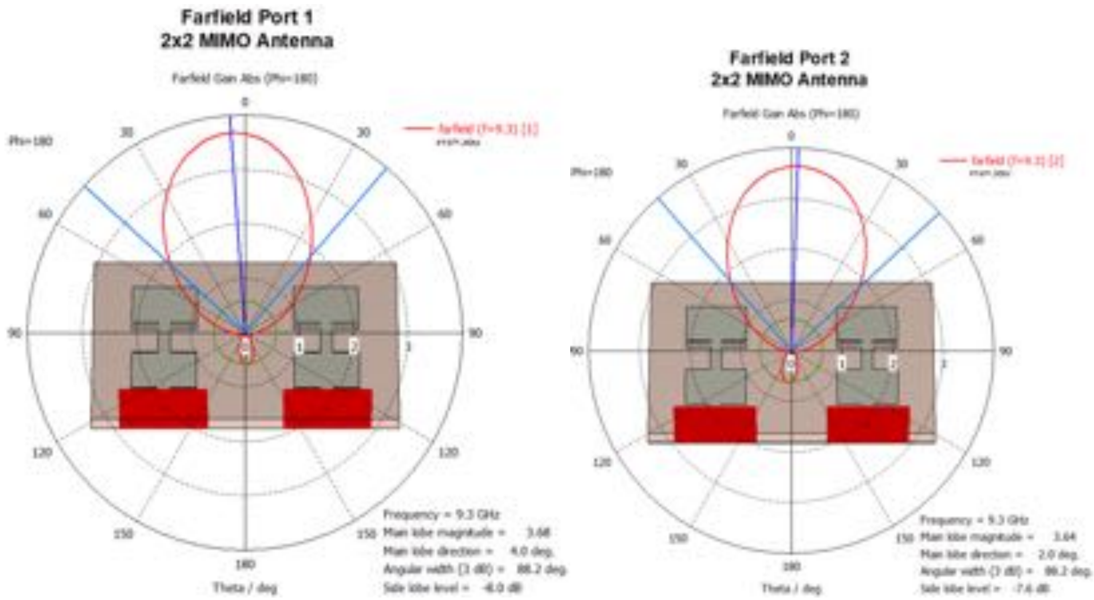

(a) (b)

Fig. 21. Simulated far-field results for π = 180° from 2x2 MIMO antenna with respective XYZ coordinate θ (z'-axis): (a) Port 1 at Y=0.8 and Z=1, and (b) Port 2 at Y=0.85 and Z=1

3.3 4x4 MIMO Antenna

The simulation of a 4x4 MIMO antenna, comprising sixteen single-element antennas, yields substantial reflection coefficient and isolation metrics at 9.3 GHz. For instance, port 1 demonstrates a reflection coefficientof -29.423 dB and isolation values ranging from -19.99 dB to -30.72 dB across other ports. Figure 22 shows simulated results of S-parameters of a 4x4 MIMO antenna.

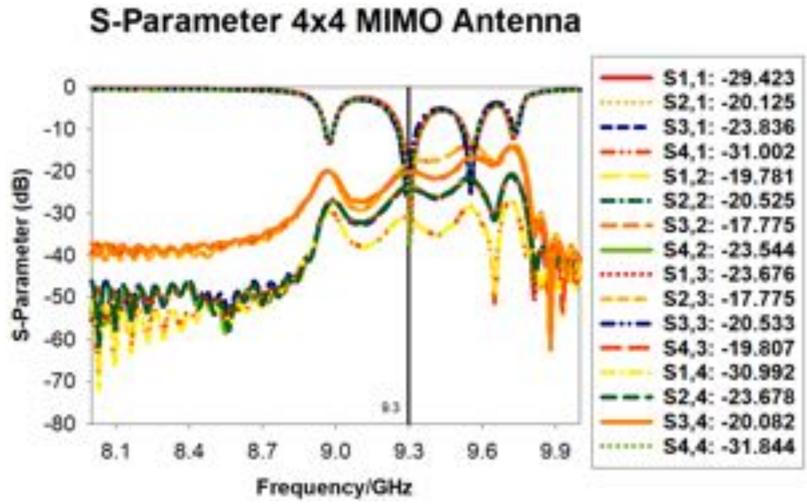

Fig. 22. Simulation result of 4x4 MIMO antenna

Additionally, far-field or radiation pattern results of 4x4 MIMO antenna shows that the main beam gain at its peak is recorded at 7.03 dBi or 5.05 W/m^2 for port 1 excitation, 6.52 dBi or 4.49 W/m^2 for port 2 excitation, 6.54 dBi or 4.51 W/m^2 for port 3 excitation, 7.1 dBi or 5.14 W/m^2 for port 4 excitation at 9.3 GHz. These results validate the antenna's capability to support high-gain and precise beamforming functionalities. Figure 23 shows simulated far-field results of a 4x4 MIMO antenna.

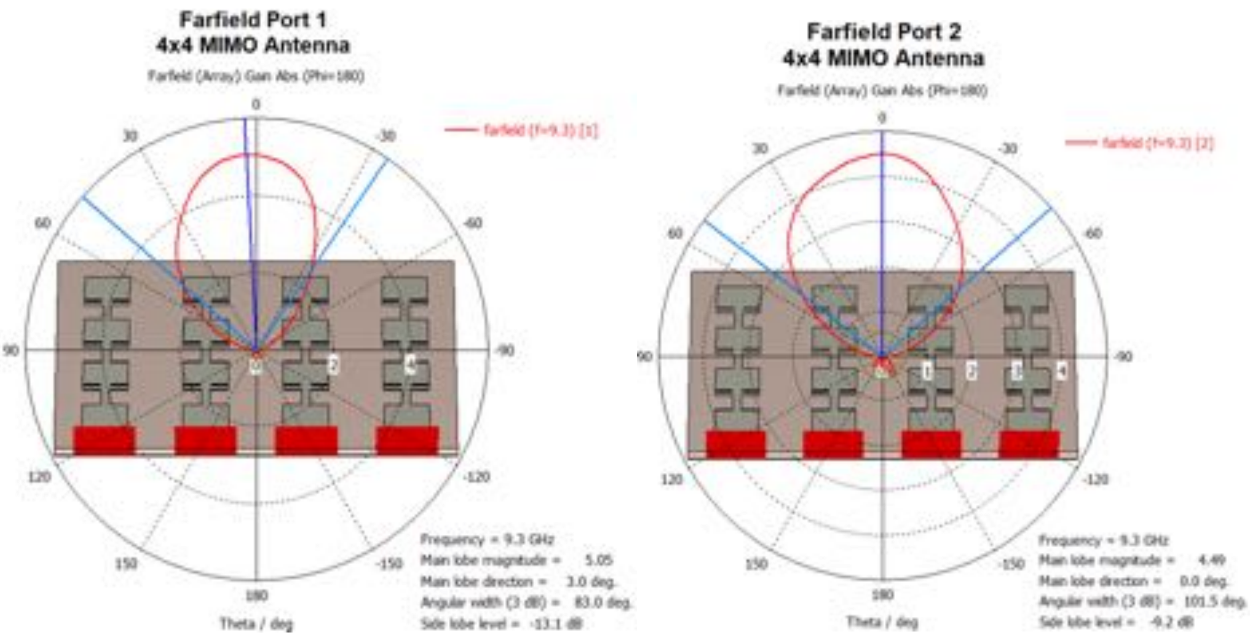

(a) (b)

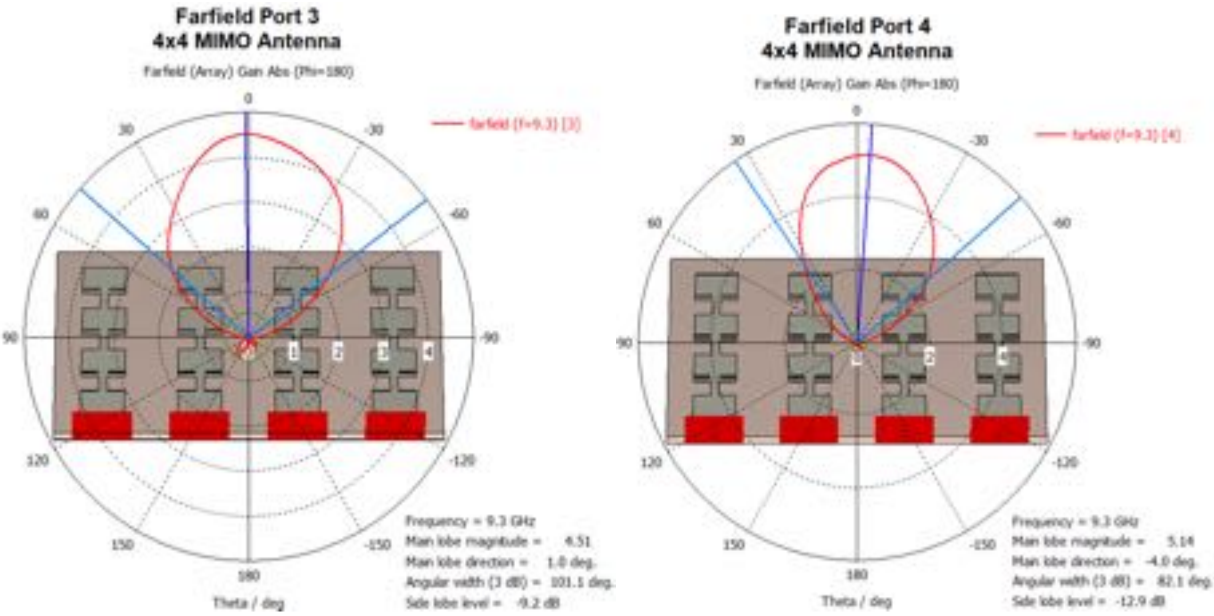

(c) (d)

Fig. 23. Simulated far-field results for π = 180° of 4x4 MIMO antenna with respective XYZ coordinate θ (z'-axis): (a) Port 1 at Y=0.72 and Z=1, (b) Port 2 at Y=0. 72 and Z=1, (c) Port 3 at Y=0. 72 and Z=1, (d) Port 4 at Y=0.73 and Z=1, and (e) Combined radiation patterns

3.4 2x2 Hybrid Coupler

The simulation results of the 2x2 hybrid coupler show that the design gives the simulation result of the power of about -3.54 dB at output ports (ports 2 and 3), which is slightly lower than the ideal hybrid coupler with a power of -3dB, but in this design, an even power is obtained between the two output ports and performs at 9.3 GHz in the X-Band frequency band. Figure 24 shows simulated results of S-parameters of a 2x2 hybrid coupler.

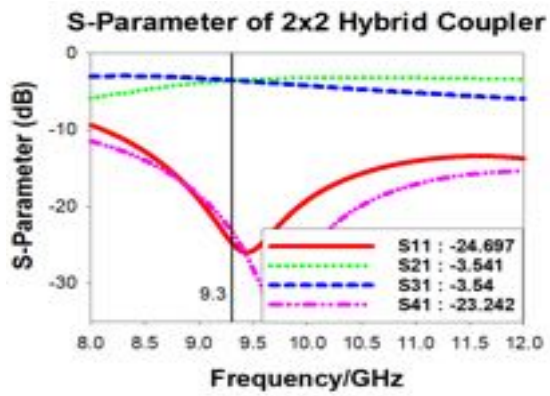

Fig. 24. Simulation results of S-parameters of a 2x2 hybrid coupler design

In addition to the S-parameter results from the design, the 2x2 hybrid coupler also shows phase difference results of about 83.864°, which has a phase error of 6.136° from the ideal hybrid coupler with a phase difference of 90°. In addition, the results show a very minimal phase deviation between port sections of <0.4°. Figure 25 shows simulation results of the phase-to-frequency response of the Butler matrix 2x2 using a mitered bend.

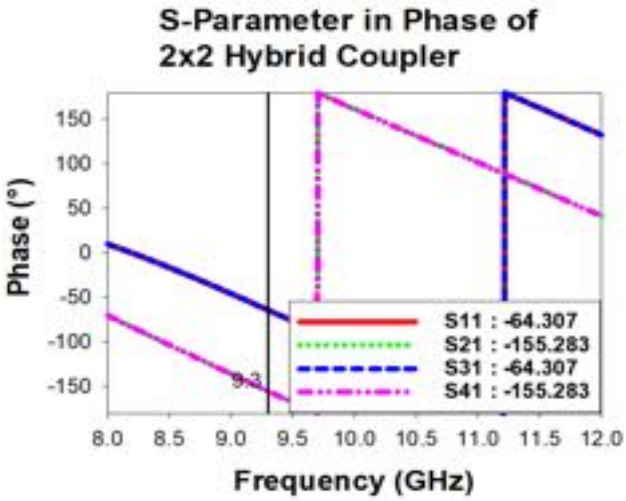

Fig. 25. Simulation results of S-parameters of the phase response to frequency of 2x2 hybrid coupler design

3.5 Crossover

The simulation results of the crossover show that the design gives a power of -1.251 dB at the output port, which is slightly below the ideal crossover with a power of 0 dB. However, this design achieved a smaller configuration that only requires a single altered 2x2 hybrid coupler than the traditional crossover that requires a cascade of two 2x2 hybrid couplers, and the design performs at 9.3 GHz. Figure 26 shows simulated S-parameters of crossover.

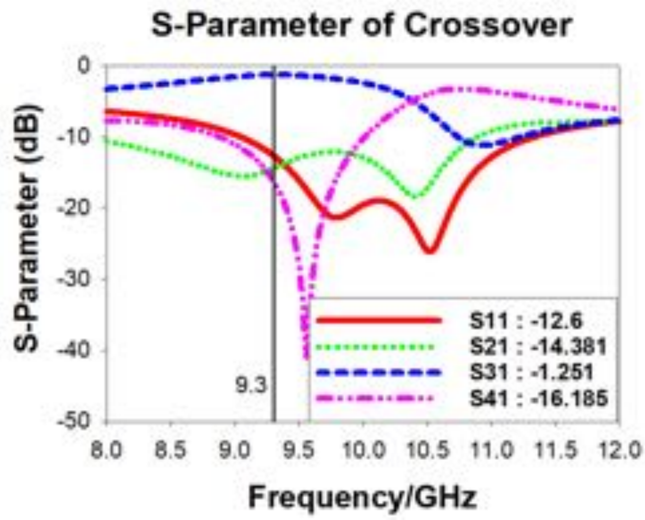

Fig. 26. Simulation results of S-Parameters of crossover design

3.6 Phase Shifter

The simulation results of the phase shifters achieved the desired phase output with overall minimal deviations. For 135° and 0° phase shifters, the simulated result shows that excitation of port 1 achieved a phase difference of around 90°, which is proportional to the passing response of the 90° hybrid coupler. The output achieved 0° phase deviation can be verified from its neighboring excitation of port 2, which gives roughly the same region phase response from the excitation of port 1 with less than 1° and 5° phase deviation for 135° and 0° phase shifter, respectively. Figure 27 depicts the simulation result of the phase towards frequency response of 135° and 0° crossover.

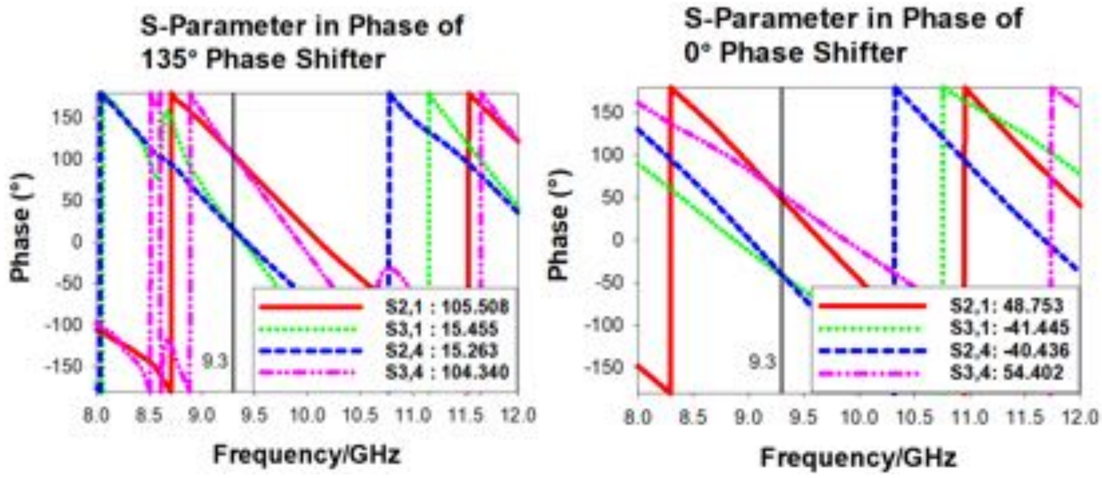

(a) (b)

Fig. 27. Simulation results of S-parameters of phase response to %the frequency of: (a) 135° crossover, and (b) 0° crossover

For the 180° phase shifter, the simulated result shows that, from excitation of port 1 achieved a phase difference of around 45° is achieved, which matches the passing response between the subtraction of the 90° hybrid coupler and the crossover that has a 135° phase response. For excitation of port 2 achieved a phase difference of around 135° was achieved, proportional to the passing response between the addition of a 90° hybrid coupler and a 45° phase shift. Figure 28 shows the simulation results of the phase-to-frequency response of the 180° crossover.

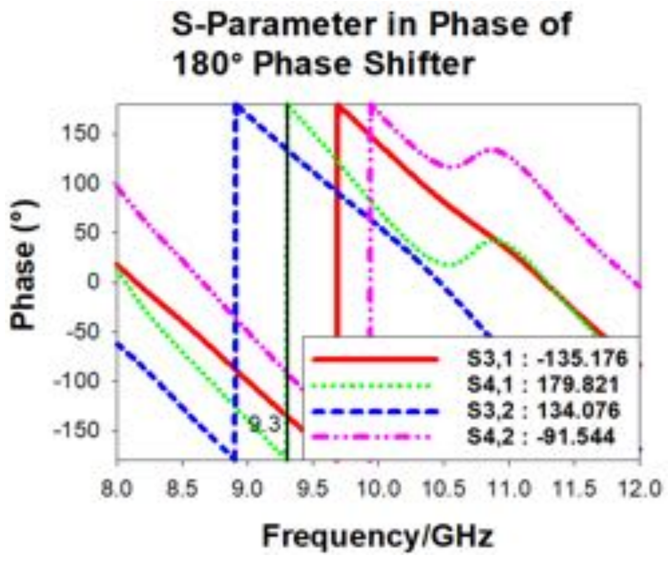

Fig. 28. Simulation results of S-Parameters of 180° crossover design

3.6 4x4 Butler Matrix

The S-parameter simulation of the conventional Butler matrix reveals strong impedance matching, with return losses for edge ports consistently below -25 dB. However, some ports demonstrate slightly higher return losses under -10 dB. Insertion loss ranges from -6.9 dB to -10.4 dB, indicating efficient signal distribution with moderate attenuation. Despite minor shortcomings in output attenuation, the matrix's beam-steering capabilities are validated, providing directional signal control. Figure 29 shows the simulation results of S-parameters of a 4x4 conventional Butler matrix.

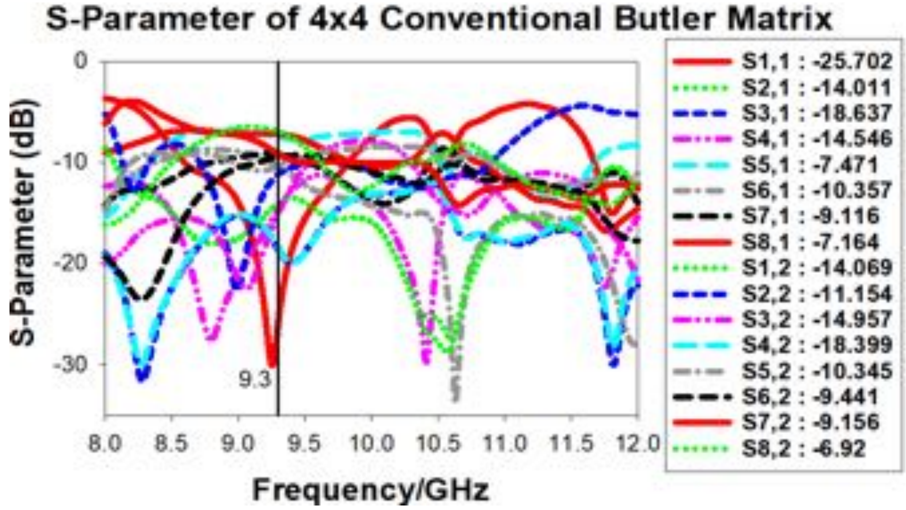

Fig. 29. Simulation results of S-Parameters of a 4x4 conventional Butler matrix

In addition to these results, the phase simulation results for the conventional configuration confirm effective beam-steering with theoretical adherence. While the phase deviation observed at the edge and middle ports highlights some irregularities, these remain within operationally acceptable ranges. Addressing these deviations through further optimization could enhance the directional precision of the matrix. Table 14 shows the S-parameter in-phase simulation result of the 4x4 conventional Butler matrix.

Table 14
4x4 conventional Butler matrix S-Parameter in the phase simulation result

Ports	1	2	3	4
5	-36.031°	-112.719°	-89.42°	-162.904°
6	-86.082°	-1.972°	144.018°	-127.553°
7	-127.572°	144.006°	-1.957°	-86.085°
8	-162.9°	-89.41°	-112.693°	-36.999°

The modified Butler matrix exhibits return losses below -10 dB for all ports, demonstrating consistent impedance matching and reduced signal reflection. The insertion loss and isolation also meet standard requirements (below -10dB), achieving efficient energy transmission. Figure 30 shows the simulation results of S-parameters of the 4x4 modified Butler matrix.

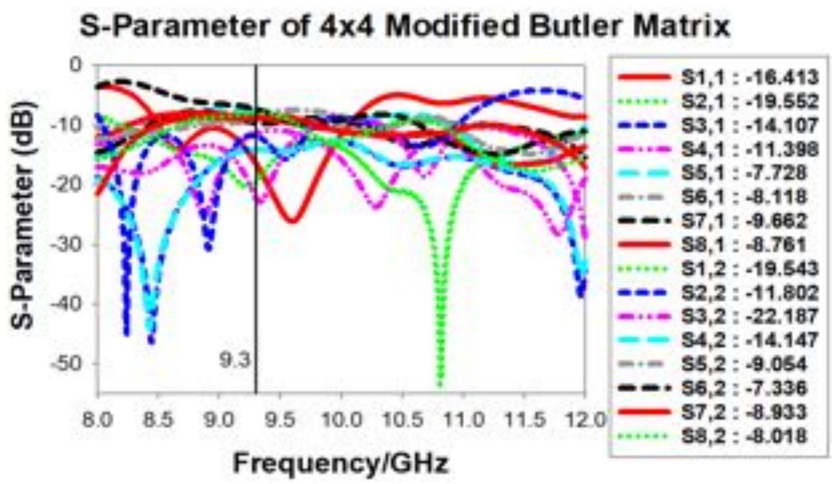

Fig. 30. Simulation results of S-Parameters of 4x4 modified Butler matrix

Despite the removal of a crossover unit, the modified configuration maintains a consistent phase response with acceptable deviations, albeit with a noticeable shift of about -45° compared to the conventional design. While flipped responses at middle ports arise due to the crossover removal, the overall phase deviation remains within operational tolerances. Table 15 shows the S-parameters in the phase simulation result of the 4x4 modified Butler matrix.

Table 15
4x4 modified Butler matrix S-Parameter in the phase simulation result

Ports	1	2	3	4
5	-93.024°	-167.926°	-138.965°	135.476°
6	-167.428°	92.259°	-47.467°	-134.415°
7	-134.408°	-47.461°	92.27°	-167.426°
8	135.485°	-138.956°	-167.918°	-93.008°

3.7 Integrated 2×2 MIMO Antenna and Butler Matrix

The integration of a 2×2 MIMO array antenna with a 2×2 Butler matrix demonstrates good impedance matching and signal isolation performance. Return losses at the input ports are recorded at -14.04 dB for S11 and -14.20 dB for S22, indicating fairly optimal impedance matching at both ports. Mutual coupling between ports is likewise solid, with S21 reaching -19.29 dB and S12 at -19.31 dB, indicating low interference between transmission channels. Figure 31 shows the simulation results of S-parameters of the integrated 2×2 MIMO array antenna and 2×2 Butler matrix.

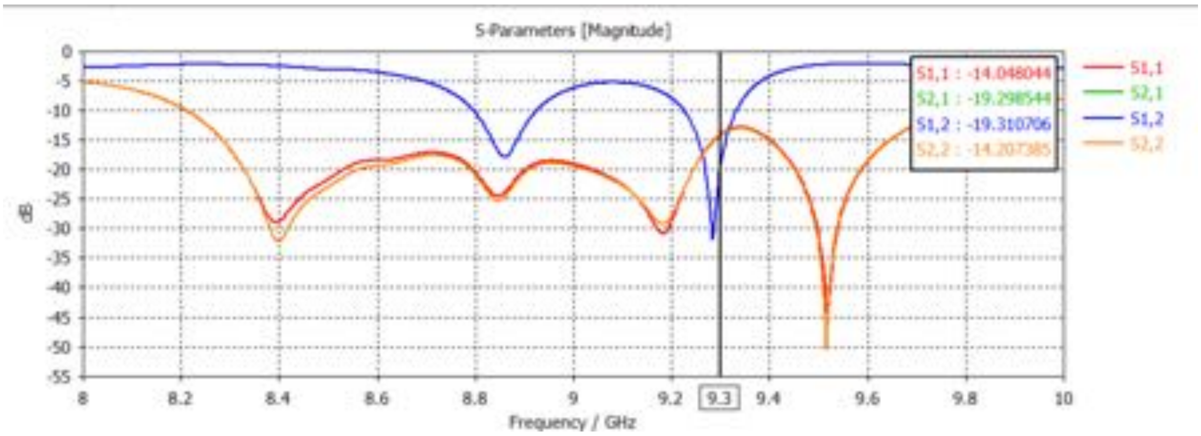

Fig. 31. Simulation results of S-Parameters of integrated 2×2 MIMO array antenna and 2×2 Butler matrix

Far-field or radiation pattern results of the integrated 2×2 MIMO array antenna with the 2×2 Butler matrix show that the main lobe direction is achieved at 20° for port 1 excitation and -20° for port 2 excitation, confirming a symmetric and consistent beam-steering distribution resulting from the phase and amplitude division performed by the Butler matrix. The main beam gain at its peak is recorded at 6.1 dBi for port 1 excitation and 6.11 dBi for port 2 excitation, a relatively small difference indicating stable and consistent power distribution across both ports. Figure 32 shows the simulation results of the radiation pattern of the integrated 2×2 MIMO antenna with the 2×2 Butler matrix.

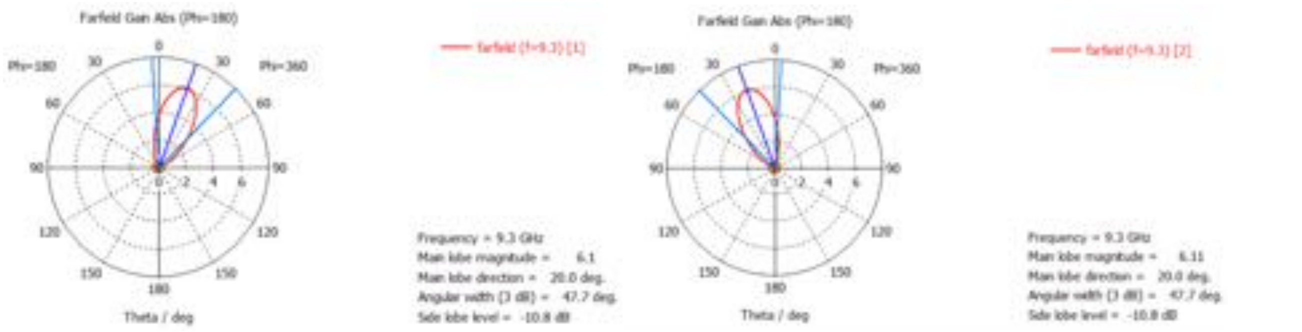

(a) (b)

Fig. 32. Simulated radiation pattern of integrated 2×2 MIMO antenna with 2×2 Butler matrix: (a) Port 1, (b) Port 2

3.8 Integrated 4x4 MIMO Antenna and Butler Matrix

This section presents the results and discussion on the performance of Multi-Beam Smart Array Antennas using 4x4 MIMO array antenna and Butler matrix with conventional and modified configurations. The performance evaluation is based on S-parameter analysis and radiation pattern simulations.

3.8.1 4x4 MIMO Array Antenna and Conventional Butler Matrix

The integration of a 4x4 MIMO array antenna with the conventional Butler matrix demonstrates effective impedance matching and signal management. Return losses for the middle ports (S22 and S33) are below -10.6 dB, while the edge ports (S11 and S44) exhibit higher return losses at around -27.3 dB. The isolation between the middle ports (S23/S32) is strong, with values ranging from -12.8 dB to around -15 dB. However, the isolation between the farthest ports (S14/S41) measures around -6.3 dB, below ideal performance thresholds. These results indicate that the conventional Butler matrix effectively supports signal distribution and isolation, though further optimization may enhance edge port performance. Figure 33 shows simulation results of S-parameters of the integrated 4x4 MIMO array antenna and conventional Butler matrix.

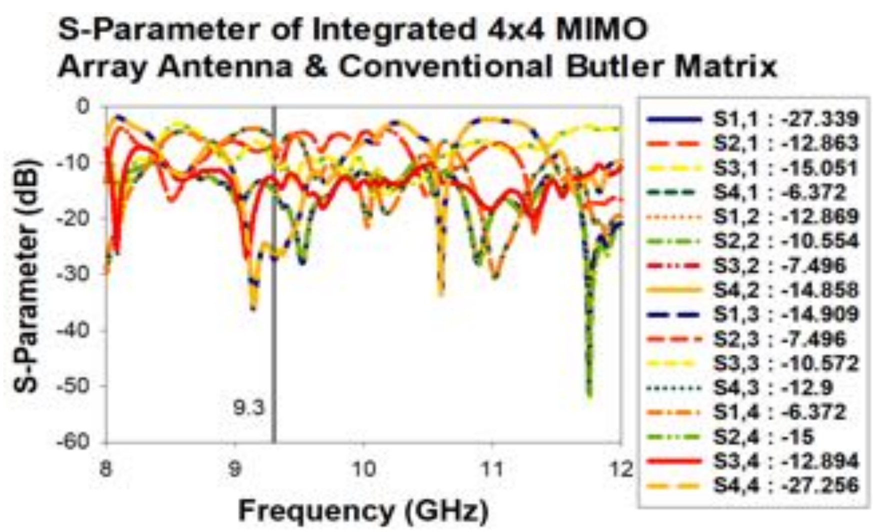

Fig. 33. Simulation results of S-Parameters of integrated 4x4 MIMO array antenna and conventional Butler matrix

Far-field or radiation pattern results of the integrated 4x4 MIMO array antenna with a conventional Butler matrix show that the main beam gain at its peak is recorded at 11.9 dBi or 15.5 W/m^2 for port 1 and 4 excitation, 9.75 dBi or 9.45 W/m^2 for port 2 excitation, and 9.76 dBi or 9.46 W/m^2 for port 3 excitation. For the main lobe directions, the tilt angle of -13°, 45°,-45°, and 13° for ports 1, 2, 3, and 4, respectively. This simulated result highlights that the configuration has weaker peak gain at middle port regions (port 2 and 3 excitations) or specifically at the outer beams and has ±2° phase deviation at the edge ports compared with the ideal ±15° and ±45° tilt angles. Figure 34 shows the simulation results of the radiation pattern of an integrated 4x4 MIMO antenna with a conventional Butler matrix.

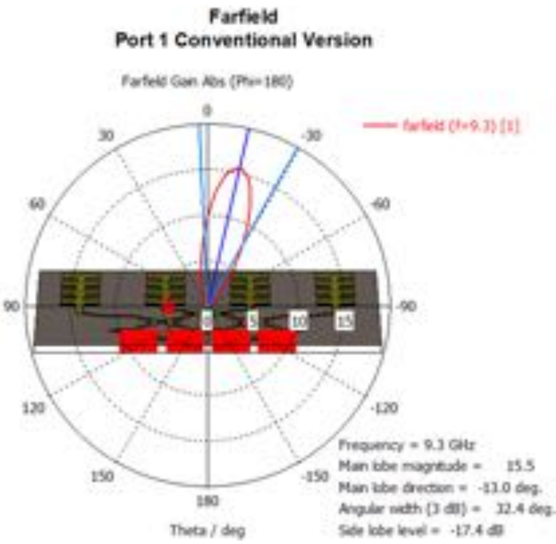

(a)

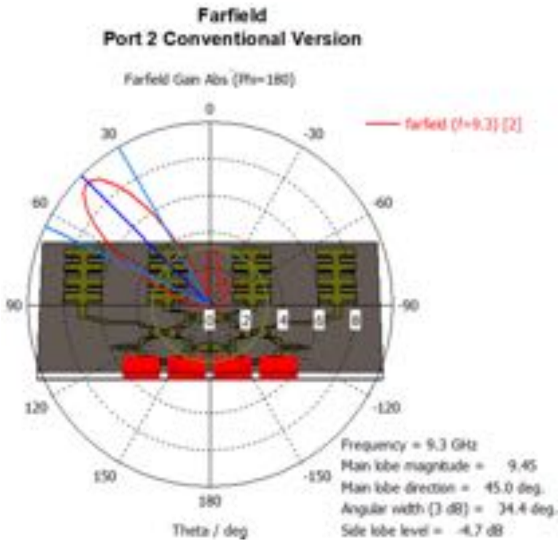

(b)

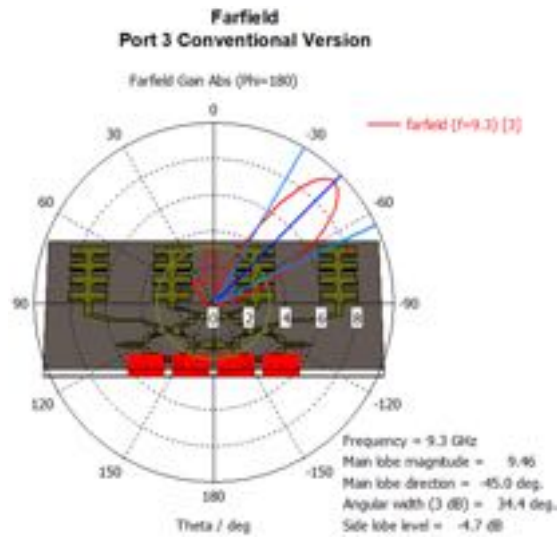

(c)

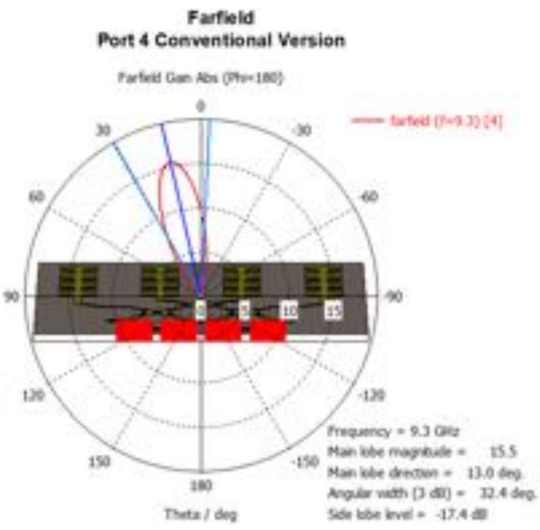

(d)

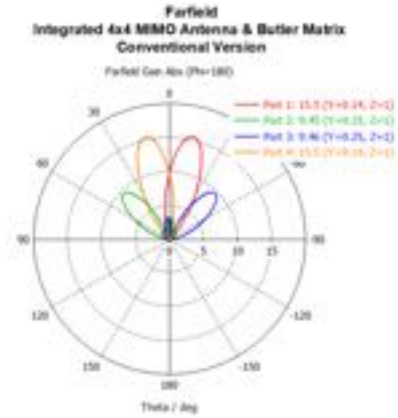

(e)

Fig. 34. Simulated far-field results for π = 180° of integrated 4x4 MIMO antenna with conventional Butler matrix with respective XYZ coordinate θ (z'-axis): (a) Port 1 at Y=0.14 and Z=1, (b) Port 2 at Y=0.25 and Z=1, (c) Port 3 at Y=0.25 and Z=1, (d) Port 4 at Y=0.14 and Z=1, and (e) Combined radiation patterns

3.8.2 4x4 MIMO Array Antenna and Modified Butler Matrix

The integration of a 4x4 MIMO array antenna with a modified Butler matrix achieves a more compact, balanced configuration compared to the conventional Butler matrix, but with weaker return losses specifically at the edge ports. Return losses for all ports (S11, S22, S33, and S44) are consistently below -12.5 dB. The isolation between the edge ports (S14/S41) is strong, with values ranging from -12.9 dB to around -21.2 dB. However, the isolation between the middle ports (S23/S32) measures around -7.2 dB, below the standard requirement. Because these values represent different port pairs than those compared in the conventional configuration, a direct like-for-like comparison shows that the modified design redistributes isolation performance across the ports rather than uniformly improving it: middle-port isolation is weaker than in the conventional design, while edge-port isolation is markedly stronger. Figure 35 shows simulation results of S-parameters of the integrated 4x4 MIMO array antenna and modified Butler matrix.

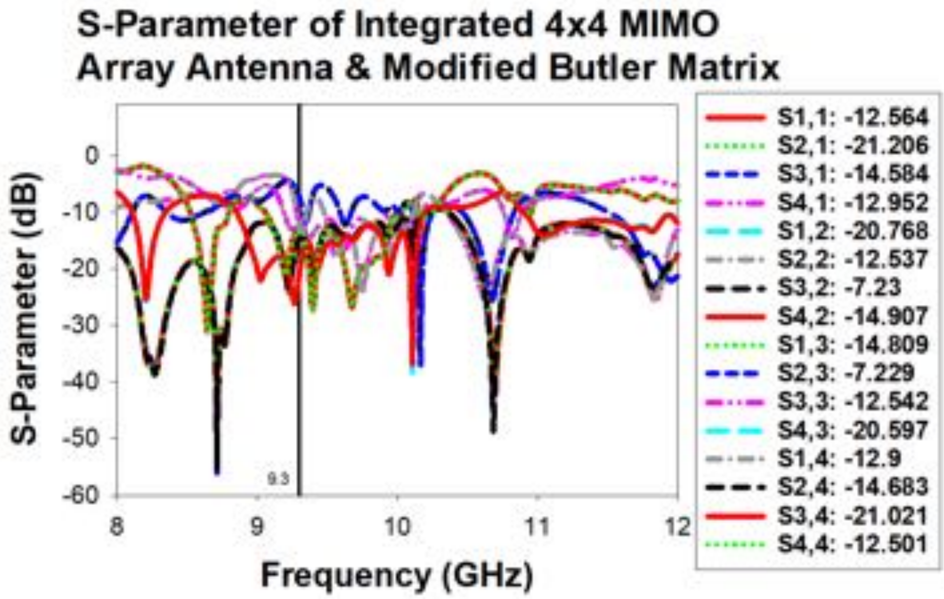

Fig. 35. Simulation results of S-Parameters of integrated 4x4 MIMO antenna and modified Butler matrix

Far-field or radiation pattern results of the integrated 4x4 MIMO array antenna with modified Butler matrix show that the main beam gain at its peak is recorded at 10.8 dBi or 12.1 W/m^2 for port 1 and 4 excitation, 10.7 dBi or 11.9 W/m^2 for port 2 excitation, and 10.7 dBi or 11.8 W/m^2 for port 3 excitation. For the main lobe directions, it is achieved at -12°, -42°,42°, and 12° for ports 1, 2, 3, and 4, respectively. This concludes that the configuration has phase deviations of ±3° across the port excitations compared with the ideal ±15° and ±45° tilt angles. This simulated result highlights that the configuration achieved balanced performance across the entire port excitations but with a slightly bigger phase deviation compared to the conventional configuration, which addresses the phase configurations that should be further reconfigured. Figure 36 shows the simulation results of the radiation pattern of an integrated 4x4 MIMO antenna with a modified Butler matrix.

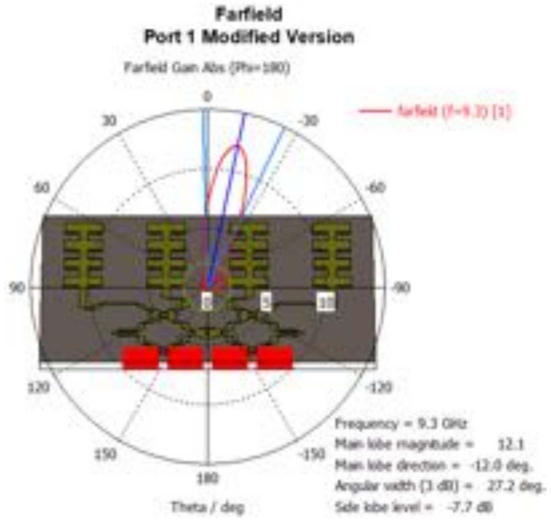

(a)

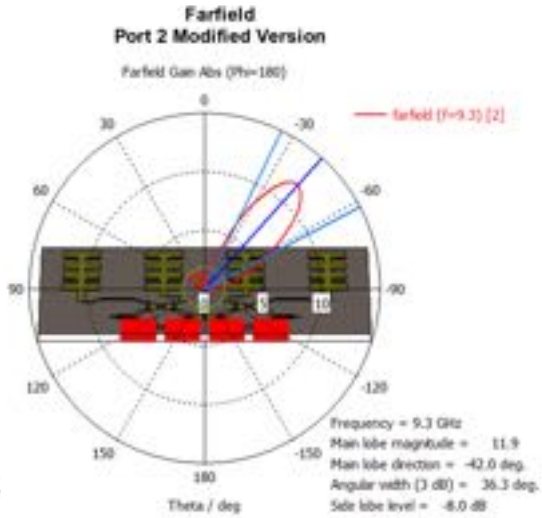

(b)

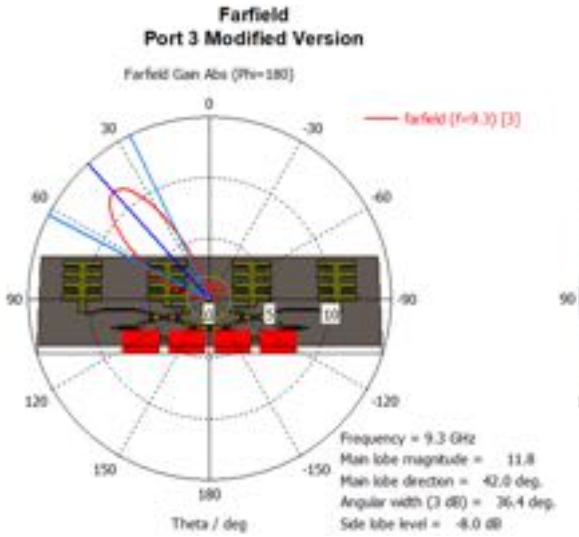

(c)

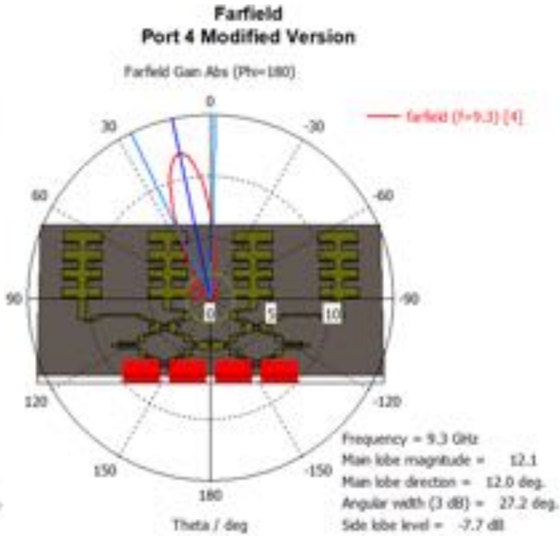

(d)

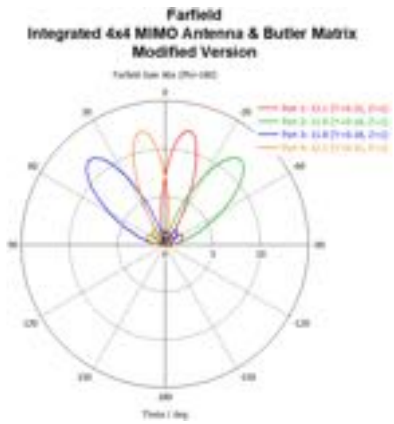

(e)

Fig. 36. Simulated far-field results for π = 180° integrated 4x4 MIMO antenna with modified Butler matrix with respective XYZ coordinate θ (z'-axis): (a) Port 1 at Y=0.31 and Z=1, (b) Port 2 at Y=0.18 and Z=1, (c) Port 3 at Y=0.18 and Z=1, (d) Port 4 at Y=0.31 and Z=1, and (e) Combined radiation patterns

3.9 Performance Comparison

Table 16 shows the performance comparison between conventional and modified Butler matrix configurations in this study. The modified configuration achieves a more compact configuration with more balanced return loss and redistributed isolation performance compared to the conventional configuration, but with a lower peak gain and larger tilt-angle deviation, as discussed in Section 4. Additionally, the modified configuration has a smaller dimension of 84.565mm x 57.18mm compared to the 89.615mm x 57.18mm conventional configuration dimension.

Table 16
Performance comparison between conventional and modified configurations

Configurations	Return Loss (dB)	Isolation (dB)	Gain (dBi)	Size (mm)	Tilt Angles
Conventional	-27.3 (S11, S44), -10.6 (S22, S33)	≈-6.3 dB, -12.8 to -15 dB	11.9 (P1, P4), 9.75 (P2), 9.76 (P3)	89.615 x 57.18	-13°, 45°,-45°, and 13°
Modified	-12.5	≈-7.2, -12.9 to -21.2	10.7 - 10.8	84.565 x 57.18	-12°, 42°,-42°, and 12°

Additionally, Table 17 shows the comparison of the proposed Butler matrix design with the existing design. The proposed design shows better results in terms of gain.

Table 17
Comparison between various 4x4 Butler matrices

Reference	[28]	[29]	[30]	[31]	This Work
Frequency (GHz)	28	3	5.2	8.3	9.3
Return Loss (dB)	>40	-24.86	>20	-34	-12.5
Isolation (dB)	NA	NA	NA	NA	Isolation
Gain (dBi)	9.8, 7.8, 10.1, 9.9	8.024	10.4	NA	10.7 - 10.8
Size (mm)	NA	6.9 × 13.69 × 1.55	46.15 × 46.15 × 2.31	53.7 x 46.7 x 1.575	84.565 x 57.18
BLC	4	4	4	4	4
Crossover	2	2	NA	2	1

3.10 Fabrication and Measurement Results

To validate the simulated designs against real-world performance, three configurations were fabricated and physically tested using a Vector Network Analyzer (VNA) ZVA 67: the single-element antenna, the 2×2 MIMO array antenna, and the 2×2 MIMO array antenna integrated with the 2×2 Butler matrix. Testing focused on return loss and radiation pattern parameters for each configuration.

3.10.1 Single-Element Antenna

After fabrication, the single-element antenna's working frequency shifted to 9.71 GHz, with a measured return loss of -14.67 dB and a bandwidth of 310 MHz. Although the resulting bandwidth falls short of the targeted specification of below 100 MHz, the return loss still meets the design criterion of below -10 dB. Figure 37 shows the measured S-parameters of the single-element antenna.

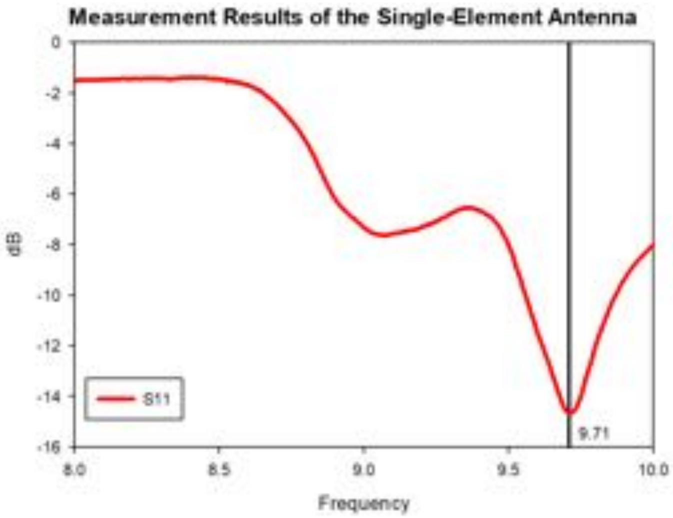

Fig. 37. Measured S-Parameters of the single-element antenna

The measured radiation pattern retains a directional characteristic consistent with the original design specification. However, a deviation is observed in the 270°–360° angular range, where the measured pattern narrows inward rather than forming the symmetric circular shape produced in simulation. Figure 38 shows the measured radiation pattern of the single-element antenna.

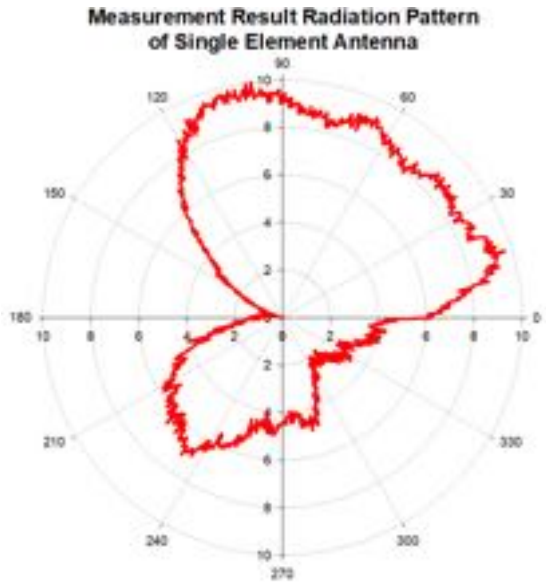

Fig. 38. Measured radiation pattern of the single-element antenna

3.10.2 2×2 MIMO Array Antenna

The fabricated 2×2 MIMO array antenna's working frequency shifted to 9.48 GHz, with a measured return loss of -24.69 dB and a bandwidth of 300 MHz. At this frequency, the measured mutual coupling was recorded at -18.61 dB, reflecting a low level of inter-element interference and indicating that signal integrity is reasonably well preserved. Figure 39 shows the measured S-parameters of the 2×2 MIMO array antenna.

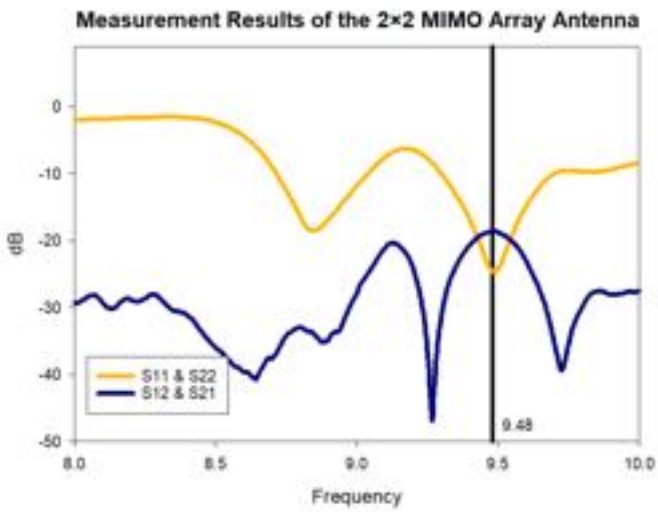

Fig. 39. Measured S-Parameters of the 2×2 MIMO array antenna

The measured radiation pattern of the 2×2 MIMO array antenna exhibits a notably wide back lobe. Although the pattern appears more dispersed than the simulated result, the main lobe direction remains identifiable, indicating that the antenna retains its directional characteristic despite the additional back-lobe radiation. Figure 40 shows the measured radiation pattern of the 2×2 MIMO array antenna.

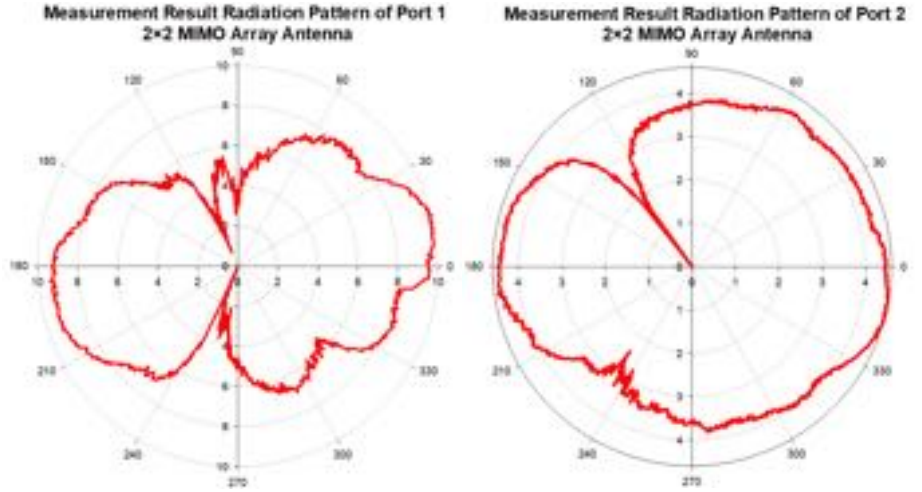

(a) (b)

Fig. 40. Measured radiation pattern of the 2×2 MIMO array antenna (a) Port 1, and (b) Port 2

3.10.3 Integrated 2×2 MIMO Array Antenna and 2×2 Butler Matrix

The fabricated and integrated 2×2 MIMO array antenna and 2×2 Butler matrix showed a working frequency shift to 9.06 GHz, with a return loss of -30.949 dB and a bandwidth of 100 MHz. Isolation performance, however, remains suboptimal: the measured mutual coupling of -10.94 dB is well above the ideal threshold of -20 dB, indicating comparatively strong inter-element interaction. Figure 41 shows the measured S-parameters of the integrated 2×2 MIMO array antenna and 2×2 Butler matrix.

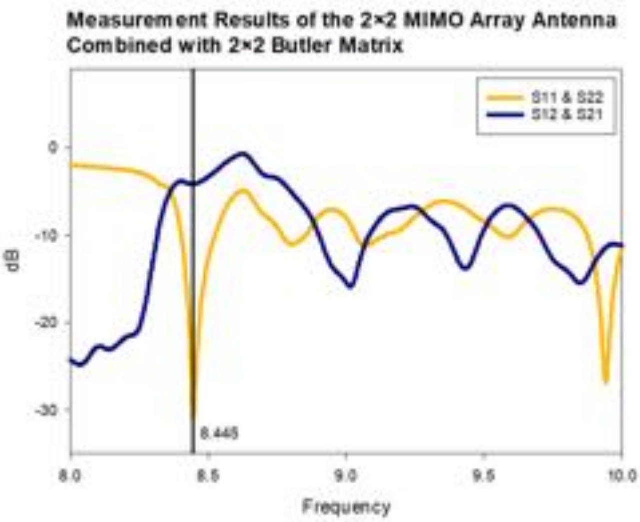

Fig. 41. Measured S-Parameters of integrated 2×2 MIMO array antenna and 2×2 Butler matrix

The measured radiation pattern shows a main lobe direction of approximately 340.39° for port 1 and 31.36° for port 2, confirming that the fabricated Butler matrix successfully performs phase shifting between output signals and steers the main beam to distinct angles without physically repositioning the antenna. Figure 42 shows the measured radiation pattern of the integrated 2×2 MIMO array antenna with the 2×2 Butler matrix.

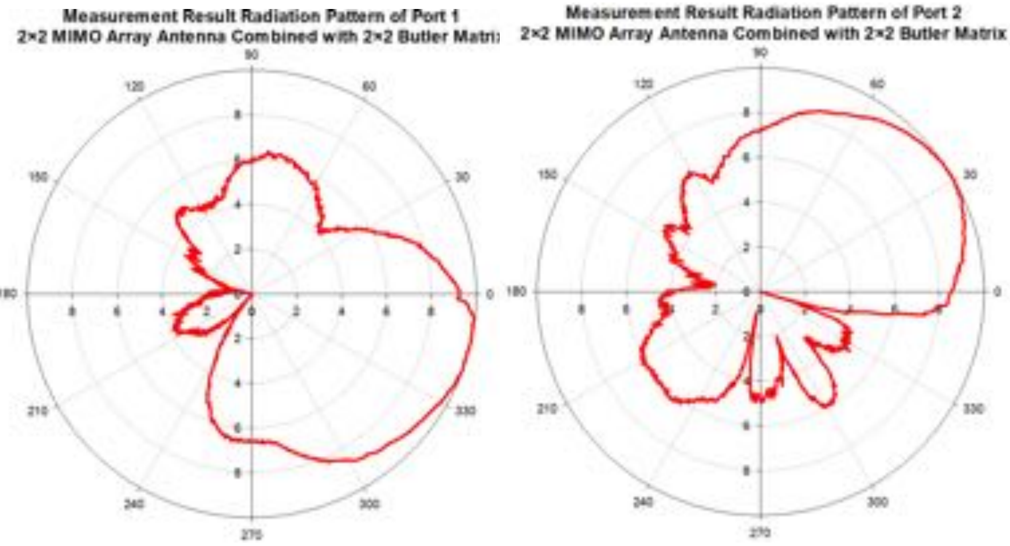

(a) (b)

Fig. 42. Measured radiation pattern of integrated 2×2 MIMO antenna with 2×2 Butler matrix: (a) Port 1, (b) Port 2

3.11 Simulation versus Measurement Comparison

Table 18 summarizes the deviation between simulated and measured performance across the three tested configurations. Across all configurations, the working frequency shifted upward or downward from the 9.3 GHz design target but remained within the X-band range, and return loss values continued to satisfy the -10 dB design criterion. The largest deviations occur in the radiation pattern parameters, which is consistent with measurements being conducted in an open environment without an anechoic chamber, allowing ambient wave reflection and interference to affect measurement accuracy. Additional contributing factors include fabrication dimensional tolerance during patch printing, connector/soldering imperfections, and impedance mismatch between the antenna, connectors, and measurement equipment.

Table 18
Comparison between *simulation versus measurement*

Configuration	Measured Frequency	Return Loss	Mutual Coupling	S11/S22 Error (%)	S12/S21 Error (%)	Radiation Pattern Error (%)
Single Element	9.71 GHz	-14.67 dB	—	15.03	—	34.00
2×2 MIMO Array	9.48 GHz	-24.69 dB	-18.61 dB	34.95	28.19	31.06 (P1), 40.33 (P2)
2×2 Array + 2×2 Butler Matrix	9.06 GHz	-30.949 dB	-10.94 dB	23.94	35.59	23.85 (P1), 28.51 (P2)

4. Conclusions

The 4x4 MIMO antenna integration with conventional and modified Butler matrices demonstrates the feasibility of multi-beam smart array antennas. The conventional configuration achieves strong edge-port return loss (-27.3 dB) and peak gains of 11.9 dBi and 9.75-9.76 dBi, but weaker farthest-port isolation (-6.3 dB) and ±2° tilt-angle deviation.

The modified Butler matrix is more compact (84.565 × 57.18 mm versus 89.615 × 57.18 mm) with consistent return loss below -12.5 dB and gains of 10.7-10.8 dBi at ±3° tilt-angle deviation. Isolation performance redistributes across ports, improving at the edge ports (-12.9 to -21.2 dB) but weakening at the middle ports (-7.2 dB) relative to the conventional design.

Despite a flipped middle-phase response from the crossover omission, both configurations maintain functional, directional radiation patterns. The comparative analysis indicates that the modified configuration involves clear trade-offs rather than an unambiguous improvement: it offers a smaller footprint, more balanced return loss across all ports, and improved edge-port isolation, but this comes at the cost of a lower peak gain (10.7-10.8 dBi versus 11.9 dBi for the conventional design), greater tilt-angle deviation (±3° versus ±2°), and weaker middle-port isolation relative to the conventional design. These findings suggest that the modified Butler matrix is best suited to applications that prioritize compactness and balanced port performance over maximum gain and tilt-angle precision. Beyond simulation, a single-element antenna, 2x2 MIMO array, and integrated 2x2 array-Butler matrix were fabricated and measured via VNA, confirming functional beam-steering at 340.39° and 31.36° and validating the crossover-reduction approach in hardware; deviations in the radiation pattern are attributable to fabrication tolerance, connector imperfections, impedance mismatch, and the non-anechoic test environment. This 2x2 validation is an essential step before scaling to a fabricated 4x4 configuration; future work should focus on this scaling, alongside improving middle-port phase accuracy, isolation, and beam-pointing accuracy.

Acknowledgment

The authors would like to thank the Indonesian Ministry of Education and Culture, Research and Technology for funding this project under the Fundamental Research Scheme 2024. The authors also thank Universitas Riau for research management and support.

References

[1] Cui, Z., P. Zhang, and S. Pollin. “6G Wireless Communications in 7-24 GHz Band: Opportunities, Techniques, and Challenges.” *arXiv.org*, October 10, 2023. https://doi.org/10.48550/arXiv.2310.06425.

[2] Neill, S. P., and M. R. Hashemi. “In Situ and Remote Methods for Resource Characterization.” In *Fundamentals of Ocean Renewable Energy*, 157–91. 2018. https://doi.org/10.1016/B978-0-12-810448-4.00007-0.

[3] Chambers, J. “Commercial X-Band: The Technical + Operational Advantages.” *MilsatMagazine*, April 2013. http://www.milsatmagazine.com/story.php?number=1530000863.

[4] National Aeronautics and Space Administration (NASA). “Chapter 6: Electromagnetics - National Aeronautics and Space Administration (NASA) Science.” NASA, 2023. https://science.nasa.gov/learn/basics-of-space-flight/chapter6-3/.

[5] Cadence PCB Solutions. “Using the X-Band and Ka-Band Frequencies for Radar Applications.” *Advanced PCB Design Blog*, March 6, 2023. https://resources.pcb.cadence.com/blog/2023-using-the-x-band-and-ka-band-frequencies-for-radar-applications.

[6] Buchwald, J., C.-P. Yeang, N. Stemeroff, J. Barton, and Q. Harrington. “Correction to: What Heinrich Hertz Discovered About Electric Waves in 1887–1888.” *Archive for History of Exact Sciences* 75, no. 2 (2020): 173–173. https://doi.org/10.1007/s00407-020-00267-8.

[7] Kementerian Koordinator Bidang Kemaritiman dan Investasi Republik Indonesia. “Menko Maritim Luncurkan Data Rujukan Wilayah Kelautan Indonesia.” August 10, 2018. https://maritim.go.id/detail/menko-maritim-luncurkan-data-rujukan-wilayah-kelautan-indonesia.

[8] Rosłoniec, S. “Range Equations of Primary and Secondary Radar Systems.” In *Fundamentals of the Radiolocation and Radionavigation*, 1–20. Springer Aerospace Technology. Springer, Cham, 2023. https://doi.org/10.1007/978-3-031-10631-6_4.

[9] Ding, K., J. Bai, and A. Kishk. “A Quasi Butler Matrix with 6×6 Beam-Forming Capacity Using 3×3 Hybrid Couplers.” In *Proceedings of the 2017 32nd General Assembly and Scientific Symposium of the International Union of Radio Science (URSI GASS)*, 1–4. 2017. https://doi.org/10.23919/URSIGASS.2017.8120341.

[10] Rahayu, Y., and J. R. M. Simanihuruk. “Design of 4x4 Butler Matrix for Beamforming 5G Antenna.” In *Proceedings of the 2021 3rd International Conference on Research and Academic Community Services (ICRACOS)*, 154–59. Surabaya, Indonesia, 2021. https://doi.org/10.1109/ICRACOS53680.2021.9701986.

[11] Liu, K., X. Bian, S. Wang, and H. Zhao. “Measurement Uncertainty of Beam Parameters Induced by Imbalances of Amplitude and Phase for Antenna Array.” In *Proceedings of the 2020 Conference on Precision Electromagnetic Measurements (CPEM)*, 1–2. Denver, CO, USA, 2020. https://doi.org/10.1109/CPEM49742.2020.9191714.

[12] Rahayu, Y., J. R. M. Simanihuruk, and Y. Wahyu. “A Compact Design of 4×4 Butler Matrix with Four Linear Array Antenna at 38 GHz.” *International Journal of Electrical, Energy and Power System Engineering* 5, no. 3 (2022): 80–85. https://doi.org/10.31258/ijeepse.5.3.80-85.

[13] Shao, Q., and F.-C. Chen. “Design of 2 × 8 Filtering Butler Matrix with Arbitrary Power Distribution.” *IEEE Transactions on Circuits and Systems II: Express Briefs* 68, no. 12 (2021): 3527–31. https://doi.org/10.1109/TCSII.2021.3078201.

[14] Rahayu, Y., and A. Ibrahim. “Investigation on Simulation-Based Octagonal Ring MIMO Antenna for 5G Applications.” In *Proceedings of the 2021 17th International Conference on Quality in Research (QIR): International Symposium on Electrical and Computer Engineering*, 191–94. Depok, Indonesia, 2021. https://doi.org/10.1109/QIR54354.2021.9716187.

[15] Paul, L. C., M. I. Hasan, R. Azim, M. R. Islam, and M. T. Islam. “Design of High Gain Microstrip Array Antenna and Beam Steering for X Band RADAR Application.” In *Proceedings of the 2020 Joint 9th International Conference on Informatics, Electronics & Vision (ICIEV) and 2020 4th International Conference on Imaging, Vision & Pattern Recognition (icIVPR)*, 1–7. Kitakyushu, Japan, 2020. https://doi.org/10.1109/ICIEVicIVPR48672.2020.9306519.

[16] Phaneendra, C. N., K. V. V. Ram, D. Naveen, L. Sreekar, and K. K. Naik. “Design a Multi-Band MIMO Patch Antenna at X, K, and Ku Band for Wireless Applications.” In *Proceedings of the 2022 Fourth International Conference on Emerging Research in Electronics, Computer Science and Technology (ICERECT)*, 1–6. Mandya, India, 2022. https://doi.org/10.1109/ICERECT56837.2022.10060667.

[17] Sahoo, G. S., and A. Ghosh. “Antenna Array Design for Higher Spectral Efficiency for Hybrid Beamforming 5G MIMO Wireless Communication System.” In *Proceedings of the 2022 IEEE Wireless Antenna and Microwave Symposium (WAMS)*, 1–5. Rourkela, India, 2022. https://doi.org/10.1109/WAMS54719.2022.9848089.

[18] Balanis, C. A. *Antenna Theory: Analysis and Design*. 3rd ed. 2005. https://www.copyright.com.

[19] Derneryd, A. G. “Design of Microstrip Patch Antenna Elements.” 1978.

[20] Rogers Corporation. “RO3010TM Laminates.” Accessed September 28, 2024. https://www.rogerscorp.com/advanced-electronics-solutions/ro3000-series-laminates/ro3010-laminates.

[21] Jain, K., and K. Gupta. “Different Substrates Used in Microstrip Patch Antenna: A Survey.” 2012. https://www.ijsr.net.

[22] Sharma, V., M. R. Yadav, and H. R. Kamath. “Design and Analysis of Microstrip Patch Antenna for X Band at 8 GHz for Different Substrate Materials FR4, Rogers 5880, and Arlon 255.” 2023.

[23] Wellandari, M., A. Firdausi, U. Umaisaroh, and M. Alaydrus. “Design of Hybrid Element Transmitarray Antenna with Beamforming at Millimeter-Wave Frequency.” In *Proceedings of the 2021 International Conference on Radar, Antenna, Microwave, Electronics, and Telecommunications (ICRAMET)*, 74–78. Bandung, Indonesia, 2021. https://doi.org/10.1109/ICRAMET53537.2021.9650461.

[24] Rahimian, A., and A. Rahimian. “Enhanced RF Steerable Beamforming Networks Based on Butler Matrix and Rotman Lens for ITS Applications.” In *Proceedings of the 2010 IEEE Region 8 International Conference on Computational Technologies in Electrical and Electronics Engineering (SIBIRCON)*, 567–72. Irkutsk, Russia, 2010. https://doi.org/10.1109/SIBIRCON.2010.5555136.

[25] Shastrakar, A., and U. S. Sutar. “Design and Simulation of Microstrip Butler Matrix Elements Operating at 2.4 GHz for Wireless Applications.” *International Journal of Scientific & Engineering Research* 7, no. 5 (2016): 1528–31. https://doi.org/10.14299.

[26] Kumar, P., and S. Roy. “Design and Performance Analysis of Ku Band Antenna Array for Satellite Communication.” *Journal of Microwave and Optoelectronics*, 2021. https://doi.org/10.1002/jmo.01234.

[27] Li, H., X. Yu, and J. Huang. “Integrated Butler Matrix with Low Insertion Loss for Multi-Beam Applications.” In *IEEE International Microwave Symposium Digest*, 1–4. 2022. https://doi.org/10.1109/IMS.2022.9815734.

[28] Aourik, S., A. Errkik, J. Zbitou, and M. Latrach. “A New Design and Implementation of 4x4 Butler Matrix for Ka Band Applications.” In *URSI GASS 2021*, Rome, Italy, August 28–September 4, 2021. https://doi.org/10.23919/URSIGASS51995.2021.9560488.

[29] Chater, Nadia, Tomader Mazri, and Mohamed Benbrahim. "Design Approach of Wideband Steerable Antenna Array Fed by Optimized 4x4 Butler Matrix." In *Proceedings of the 2020 IEEE 10th International Conference on Intelligent Data Acquisition and Advanced Computing Systems: Technology and Applications (IDAACS)*. https://doi.org/10.1109/IDAACS-SWS50031.2020.9297099.
[30] Temga, Jean, Takashi Shiba, and Noriharu Suematsu. "A Compact 2-D Phased Array Fed by 4×4 Butler Matrix Without Crossover in Broadside Coupled Stripline For Sub-6GHz 5G Applications." In *Proceedings of the 52nd European Microwave Conference (EuMC)*, 540–43. Milan, Italy, September 27–29, 2022.
[31] Khan, Osama Ullah. "Design of X-band 4x4 Butler Matrix for Microstrip Patch Antenna Array." NED University of Engineering & Technology, 2021. https://doi.org/10.1109/ICRACOS53680.2021.9701986.